Towards Comprehensive Characterisation and Modelling of the Forming and Wrinkling Mechanics of Engineering Fabrics

Harrison, P.[a*], Alvarez, M.F.[a] and Anderson, D.[a]

[a]*University of Glasgow, School of Engineering, University Avenue, Glasgow, G12 8QQ, UK*

*corresponding author: Philip.harrison@glasgow.ac.uk

Abstract

Through a combination of direct measurement and inverse modelling, a route to characterising the main mechanical forming properties of engineering fabric is demonstrated. The process involves just two experimental tests, a cantilever bending test and a modified version of the uniaxial bias extension test. The mechanical forming properties of a twill weave carbon fabric have been determined, including estimates of the in-plane bending stiffness and the torsional stiffness of a sheared fabric. As a result of measuring and incorporating all the main mechanical properties of the fabric in forming simulations (tensile, shear, out-of-plane bending, in-plane bending & torsion), the specimen size-dependent shear kinematics and wrinkling response measured in experiments, is faithfully reproduced in simulations of the uniaxial bias extension (UBE) test.

Keywords: Forming, Fabric, Wrinkling, Cantilever Bending, Shear deformation, Modelling

1 Introduction

Computer simulation of the large deformation forming mechanics of engineering fabrics (e.g. glass and carbon) is an important topic due to the role of engineering fabrics in manufacturing advanced composite parts (Long, 2005; Boisse, 2011). This investigation

demonstrates an approach to characterising their mechanical forming properties using a combination of experimental testing and inverse modelling. A semi-discrete modelling approach implemented within a commercial finite element code (Abaqus Explicit^{TM}) is employed, involving the use of a 'mutually constrained pantographic beam and membrane mesh' (Harrison, 2016). The approach is of interest due to its ability to independently control:

- the tensile stiffness in each of the two fibre directions (Boisse et al., 2001; Potluri and Thammandra, 2007)
- the fabric shear stiffness (resistance to trellis shear) (Boisse et al., 2016; Cao et al., 2008; Harrison et al., 2012, 2008)
- the out-of-plane bending stiffness in each of the two fibre directions (Cooper, 1960; de Bilbao et al., 2010; Harrison, 2016; Hu, 2004; ISO, 1998; Lammens et al., 2014; Lomov et al., 2003; Peirce, 1930; Plaut, 2015)
- the in-plane bending stiffness in each of the two fibre directions (D'Agostino et al., 2015; Dell'Isola and Steigmann, 2014; Ferretti et al., 2014; Giorgio, 2016; Giorgio et al., 2016; Harrison, 2016; Scerrato et al., 2016; Steigmann and Dell'Isola, 2015; Turco et al., 2016)
- the torsional stiffness in each of the two fibre directions (Cooper, 1960; D'Agostino et al., 2015; Giorgio, 2016; Giorgio et al., 2016; Lomov and Verpoest, 2006; Steigmann and Dell'Isola, 2015)
- inter-ply and tool-ply friction (Sachs et al., 2014)
- the thickness of the sheet (Chen and Ye, 2006; Pazmino et al., 2014)

In this investigation, experimental identification of the shear stiffness, out-of-plane bending, in-plane bending and torsional stiffness is demonstrated using just two simple tests; a cantilever bending test (Cooper, 1960; Harrison, 2016; Hu, 2004; Lammens et al., 2014; Peirce, 1930; Plaut, 2015) and a modified version of the uniaxial bias extension (UBE) test (Boisse et al., 2016; Cao et al., 2008; Harrison, 2016). Out-of plane bending stiffness in the two fibre directions and shear stiffness are direct measurements while in-plane bending and torsional stiffness are determined via inverse analysis. The structure of the remainder of this paper is as follows; the fabric employed in the investigation is described in Section 2,

experimental test methods and results are discussed in Section 3, the modelling approach is outlined in Section 4, material parameters are determined in Section 5 and conclusions of the investigation are presented in Section 6.

2 Untreated and Treated Carbon Fabric

The formability of a 2x2 twill-weave carbon fabric (see Figure 1) has been characterised in an untreated state and post treatment for analysis using Digital Image Correlation (DIC). The width of warp & weft tow width of the carbon fabric (EasyComposites, product code = CF-22-200-150,) is 2.00 +/- 0.01 and 1.92 +/- 0.05mm respectively, see Figure 1. Measurements obtained via compression testing using square plates measuring 50x50mm fitted in a Zwick universal test machine with a 2kN load cell suggested that at a low compressive stress of 1kPa, the thickness of the carbon fabric is 0.35 +/-0.01mm when measured using a single layer and 0.30 +/-0.02mm when measuring 4 stacked layers. The reduction in thickness per ply when measuring multiple plies is probably related to nesting of the fabric layers (Chen and Ye, 2006). At 100kPa the fabric was compressed to around 0.24 +/-0.01mm per layer when measuring 4 stacked layers. The areal density was 203.1 +/- 1.25 gm^{-2} prior to treatment for analysis using stereoscopic DIC and 210.9 +/- 5.5 gm^{-2} after treatment (see Section 2.1).

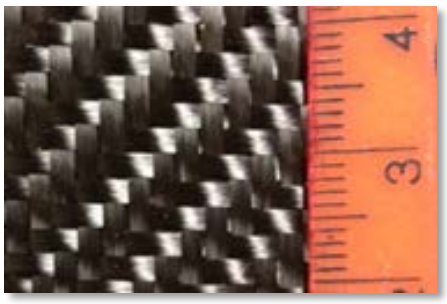

Figure 1. Twill weave carbon fabric (scale rule shows cm units).

2.1 Fabric Treatment for Digital Image Correlation (DIC) Analysis

Digital Image Correlation (DIC) has become an established technique in characterising the formability of engineering fabrics e.g. (Carvelli et al., 2012; Pazmino et al., 2015; Pierce et al., 2015; Willems et al., 2009). It is typically used to measure the shear angle of the fabric, though in this investigation, 3-D stereoscopic DIC is used to measure out-of-plane

displacements during UBE testing. The process of treating the carbon fabric for DIC inevitably changes the fabric's mechanical properties. In order to conduct DIC analysis, a non-reflective surface covered with a random, high contrast speckle pattern is preferred. Reflections from carbon fabric can cause problems with DIC analysis; the software can lose track of the speckle pattern. Use of a matt black paint can eliminate this problem though this treatment significantly changes the mechanical properties of the fabric. Instead, in this investigation, graphite powder brushed on the carbon fabric was found to eliminate reflections without stiffening the fabric. A speckle pattern was then applied by sputtering the graphite-treated surface with high viscosity white paint (e.g. Pebeo Acrylic); some degree of undesirable fabric stiffening is introduced at this stage and for this reason, the mechanical behaviour of the carbon fabric both pre and post treatment has been characterised using the test methods discussed in Section 3. A VIC 3-D DIC system was used with two video cameras. VIC-3D 2010 software (Correlated Solutions, 2010) was used to analyse the videos. A kernel size of 14x14 and Gaussian smoothing were used to analyse the data.

3 Experimental Testing and Results

The modelling approach used in this investigation requires just two characterisation test methods in order to identify the relevant mechanical parameters. In this section, each test method is presented, together with results.

3.1 Cantilever Bending Test: Method

Out-of-plane bending is an important measurement as it can be used to estimate both the out-of-plane bending stiffness in the two fibre directions as well as the torsional stiffness of the un-sheared carbon fabric (see Section 5.3) (Cooper, 1960; Hu, 2004). The cantilever test method follows the British Standard (ISO, 1998). Specimens were cut in the warp, weft and bias (45^{o}) directions. The width of the specimens was 25mm for most tests, though wide test specimens (100 mm) were also conducted for specimens cut in the bias direction to improve fabric integrity. For each direction (warp, weft and bias), each sample was tested in four different orientations, and six repeat tests in these four orientations were performed, as suggested in the British Standard (ISO, 1998). The out-of-plane flexural rigidity per unit width (given in the units Nm) is found by measuring the length of fabric, L_s, overhanging a

slope which has a gradient of $\phi = 41.5^{o}$ to the horizontal (see Figure 2), together with the weight of the fabric per unit area, *p*.

Figure 2. Bending test rig showing a fabric specimen, a ruler with rubber bonder to underside and the 41.5° slope, image reproduced from Harrison (2016).

The main equation of the standard is used to determine the effective bending stiffness per unit width (in any direction) and is based on the work of Peirce (1930). The solution can be written as:

$$\beta = \frac{pL_s^3}{8} \qquad (1)$$

where β is the out-of-plane flexural rigidity per unit width (given in the units Nm), *p* is the mass per unit area (areal density) multiplied by the acceleration due to gravity, taken here to be 9.81ms^{-2} and L_s is the cantilever strip length. The technique allows only a single value of the out-of-plane flexural modulus to be determined for any given direction. The test method was discussed recently in Harrison (2016) and is expected to provide an accuracy of around 0.3% per cent for the curvature created during the test. Note that the bending stiffness of engineering fabrics tends to decrease with increasing curvature (de Bilbao et al., 2010; Liang et al., 2014; Lomov et al., 2003) nevertheless, a single value for each fibre direction is sufficient for the purpose of this investigation.

3.2 Cantilever Bending Test: Experimental Results

Values of the overhang length, L_s, in the two fibre directions and in the bias direction (where *i* = 1, 2 or 45 corresponds to the warp, weft and bias directions), were measured and the out-of-plane bending stiffness per unit width, β_i, was calculated using Eq (1). Results for

both untreated and treated samples are shown in Figure 3 (error bars indicate +/-1 standard deviation). Both untreated and treated fabrics are slightly unbalanced with out-of-plane bending stiffness in the warp direction about 27% higher than in the weft direction. The reason for the slight asymmetry is not clear, though might possibly be attributable to small differences in the crimp in the two fibre directions resulting from unequal tensions in the warp and weft tows during weaving (Lomov et al., 2000). However, no noticeable difference in crimp in the two directions could be discerned to verify this hypothesis. Investigation into this effect is deferred to future work. Out-of-plane bending stiffness in the bias direction was considerably lower than in either of the two fibre directions. Also, the DIC treatment process increases the stiffness in both warp and weft directions by about 36% and by about 23% in the bias direction. Due to concerns relating to the fragility and integrity of relatively narrow 25mm samples cut in the bias direction (Gatouillat et al., 2013), 100mm wide samples were also tested. This change in specimen width increased the measured value of β_{45}, for both the untreated and treated samples by a factor of around two, confirming that improvements of the integrity of the specimens cut in the bias direction increases their out-of-plane bending stiffness. The wider specimens are used as the more representative value of β_{45} for the fabric. Further interpretation of these out-of-plane bending results is provided in Section 5.4.

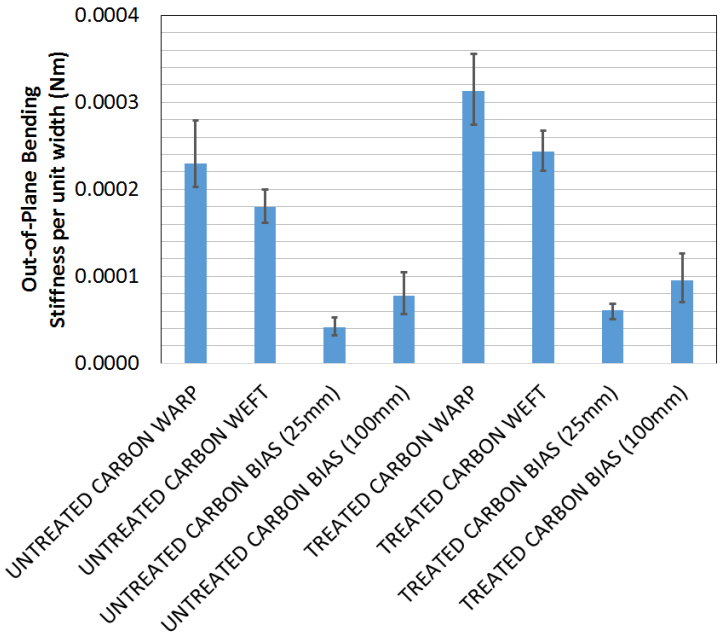

Figure 3. Out of plane bending stiffness determined using Eq (1). Error bars indicate +/-1 standard deviation from average value.

3.3 Uniaxial Bias Extension (UBE) Test: Method

The uniaxial bias extension (UBE) test is typically used to measure the shear compliance of engineering fabrics and prepregs (Boisse et al., 2016; Cao et al., 2008; Harrison et al., 2012, 2008; Machado et al., 2016). In this investigation it will also be employed to identify both the in-plane bending stiffness (D'Agostino et al., 2015; Dell'Isola and Steigmann, 2014; Ferretti et al., 2014; Giorgio et al., 2016; Harrison, 2016; Scerrato et al., 2016; Turco et al., 2016) and the torsional stiffness of the sheared fabric (Lomov and Verpoest, 2006; Steigmann and Dell'Isola, 2015) by monitoring the sample kinematics, including the shear angle at the centre of the specimen (D'Agostino et al., 2015; Ferretti et al., 2014; Harrison, 2016) and the out-of-plane wrinkling behaviour (Arnold et al., 2016; Boisse et al., 2011; Cherouat and Billoët, 2001; Dangora et al., 2015; Harrison, 2016; ten Thije and Akkerman, 2009; Thompson et al., 2016).

A Zwick universal test machine fitted with a 2kN load cell was used for the tests. The UBE test has been discussed extensively in the literature (Boisse et al., 2016; Cao et al., 2008; Harrison et al., 2008; Machado et al., 2016) and involves clamping a piece of biaxial fabric such that the warp and weft tows are orientated initially at +/- 45^{o} to the direction of the applied tensile force. The sample's length / width ratio ($\lambda = L/W$), must be at least two. L_A is the side length of Region A (see Figure 4a) and is used later to normalise axial force data. Figure 4a shows an idealised UBE test sample with $\lambda = 2$ in which the material is divided into three regions. If the tows within the sample are considered inextensible, no intra-ply slip (Bel et al., 2012; Cao et al., 2008; Harrison et al., 2005; Pan et al., 2015; Potter, 2002) occurs within the sample and the in-plane bending stiffness of the fabric is zero, then the shear angle in Region A is always twice that in Region B, while Region C remains un-deformed, see Figure 4b.

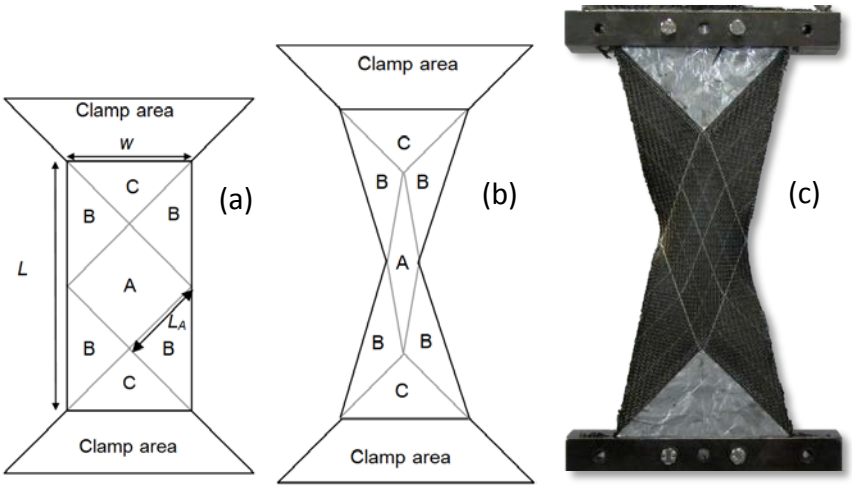

Figure 4. (a) An idealised UBE test sample with $\lambda = L/w = 2$, (b) ideal geometry of specimen during test and (c) a modified UBE test with aluminium foil bonded onto Region C of a 150 x 300 mm carbon fabric specimen.

In this investigation, a simple but important modification to the usual UBE test is introduced; aluminium foil is bonded to the fabric in Region C (see Figure 4c) and to the clamping areas shown in Figure 4a & 4b using epoxy adhesive (Permabond ET500). All UBE tests were conducted using a crosshead displacement rate of 200mm per minute. The main goal of bonding aluminium foil is to mitigate sample deformation (intra-ply slip) in Region C and to provide a well-defined 'encastre' boundary condition along the edge of Region C. A short preliminary investigation into the influence of the bonded aluminium sheet as a function of specimen size was conducted; results are discussed in Appendix A and demonstrate the technique is very effective in mitigating intra-ply slip in Region C. (The technique also facilitates the drilling of holes in the clamping area for subsequent placement of clamping bolts, a process that can otherwise deform and damage the test specimen). Metallic gold marker pen was used to highlight the fibre directions on the fabric specimen (see Figure 4c). Videos of each test were recorded using a Casio HS EX-ZR700 digital camera positioned orthogonally and directly in front of the specimen. From the videos, images were captured at specific time intervals and manual image analysis was performed using Imagej (Ferreira and Rasband, 2012) to correlate the crosshead displacement and the shear angle at the centre of Region A of the sample. Prevention of slip in Region C means that the ideal shear angle can be determined directly from the crosshead displacement and the initial shear angle in Region A using,

$$\theta = \frac{\pi}{2} - 2acos\left[\frac{d}{2(\lambda-1)L_A} + cos\frac{\emptyset_o}{2}\right] \quad (2)$$

where θ is the shear angle, $\emptyset_0$ is the initial inter-fibre angle at the centre of the specimen at the start of the test (ideally this would be 90° but rarely exactly is, adjustment to account for this discrepancy is important in achieving accurate results) and L_A is the side length of Region A (see Figure 4a). The underlying shear force per unit length versus shear angle curve required for finite element simulations can be estimated using stress-power based normalisation theory (Harrison and Hartel, 2016), i.e.,

$$F_{sh}(\theta) = \frac{(\lambda-1)}{\sqrt{2}\cdot W(2\lambda-3)} \cdot \frac{F_{be}(\theta)}{cos(\pi/4-\theta/2)} - \frac{F_{sh}(\theta/2)}{(2\lambda-3)} \cdot \frac{[sin(\pi/4-\theta/4)]}{[sin(\pi/4-\theta/2)]} \cdot \frac{[cos(\pi/4-\theta/4)]}{[cos(\pi/4-\theta/2)]} \quad (3)$$

where F_{be} is the axial force measured in the test, θ is the shear angle in Region A and F_{sh} is the shear force versus shear angle per unit side length of the fabric (see Eq (1) in Harrison et al., 2008). An iterative algorithm is required to determine F_{sh} (Harrison et al., 2008).

3.4 Uniaxial Bias Extension Test: Experimental Results

Various measurements taken during the UBE test designed to understand the shear stiffness, in-plane bending stiffness and torsional stiffness of the fabric during shear are presented in this section. All carbon fabric specimens were prepared with aluminium bonded on Region C (see Figure 4c). Carbon fabric specimens measuring 100x200, 150x300 and 200x400mm were tested (2 repeats per specimen size). Axial force was recorded via the load-cell of the test machine and videos of the tests were used to monitor the sample kinematics (see Section 3.3).

3.4.1 Measurement of Axial Force

Axial force is an important measurement as it can be used to estimate the shear stiffness of the sheared carbon fabric using Eq (3). The axial force was measured for both the untreated and treated carbon fabric. Axial force data were initially normalised by dividing the force by L_A, the side length of Region A, to facilitate direct comparison of results obtained from tests using different specimen sizes. The data points in Figure 5 shows the normalised axial force versus the measured shear angle at the centre of Region A. The measured shear angle was taken directly from video footage of the test using image analysis software (Ferreira and Rasband, 2012). Figure 5(a-c) are from the untreated fabric, Figures 5(d-f) are from the treated fabric. The data points show the normalised axial force of the treated carbon fabric

is higher (by around 1.6-2x, depending on specimen size) than the untreated fabric, demonstrating the influence of the speckle pattern treatment on the fabric's mechanical shear properties. The red lines and blue dotted line in Figure 5 are axial force predictions from simulations of the UBE test and are discussed further in Section 5.4.

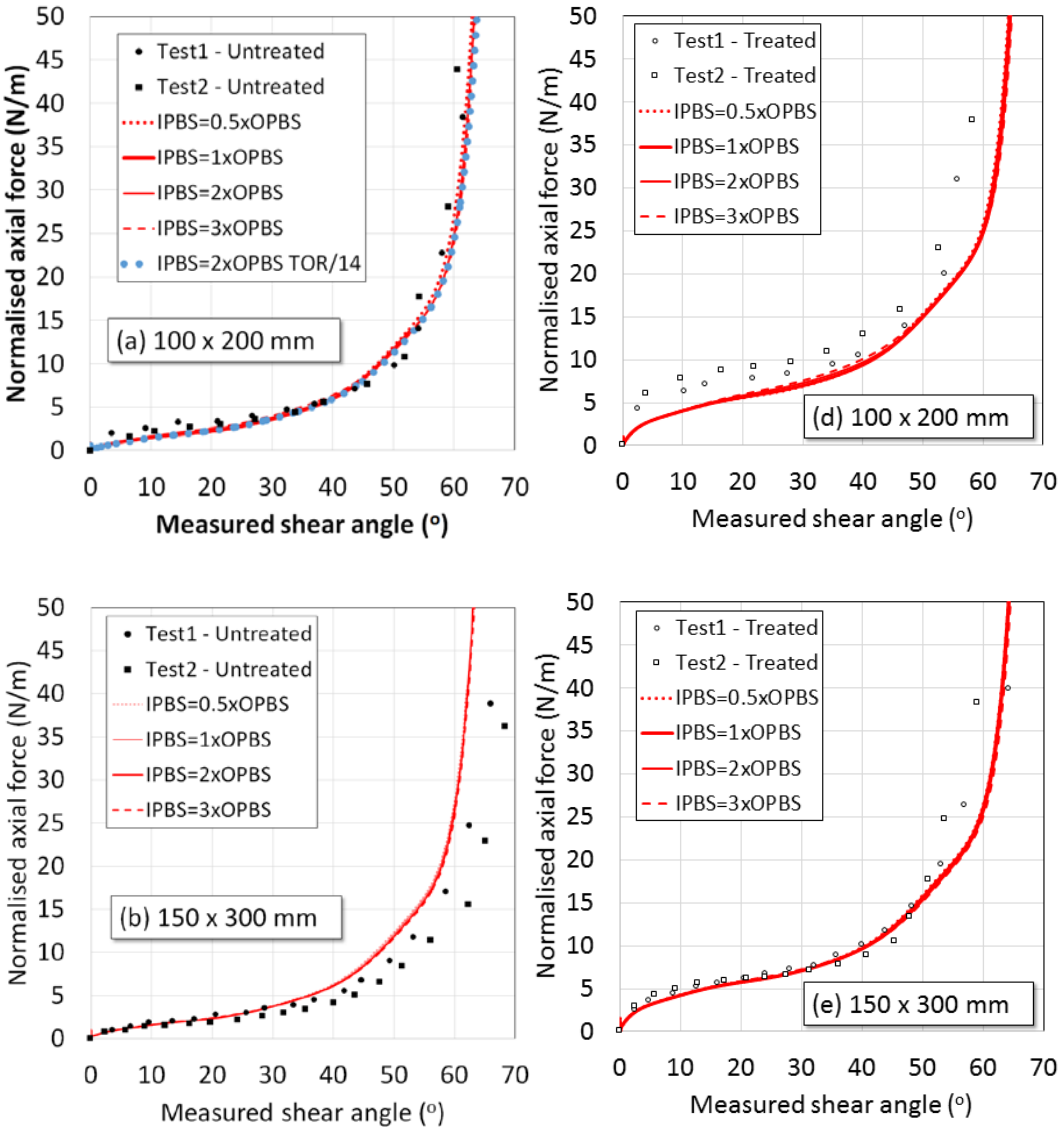

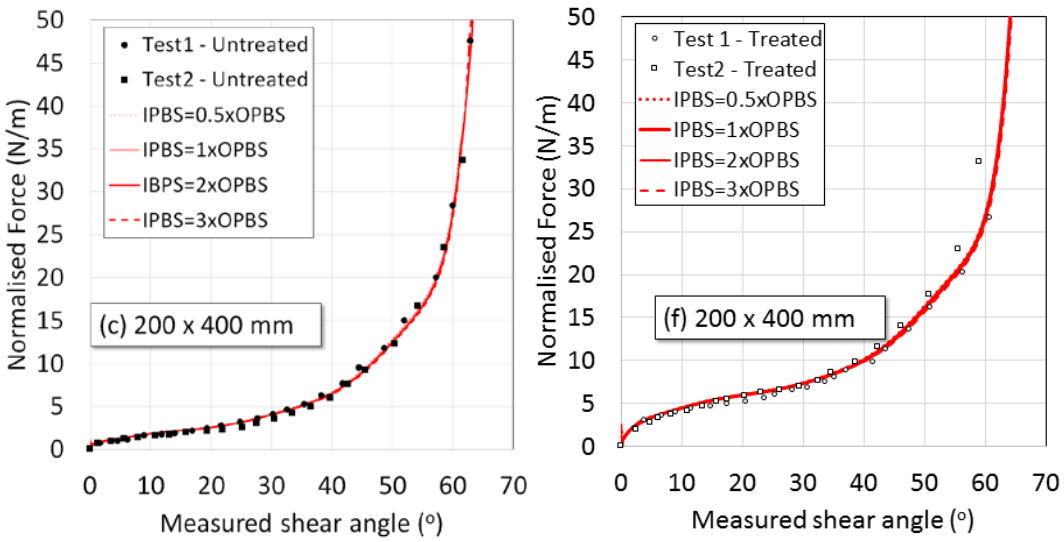

Figure 5. Axial force normalised by the side length of Region A for different sized samples: (a-c) untreated carbon fabric (d-f) treated carbon fabric. The red lines are from simulations (see Section 5.4). In the legend IPBS is the in-plane bending stiffness per unit width and OPBS is the out-of-plane bending stiffness per unit width and TOR represents the modification factor of the default torsional stiffness per unit width.

3.4.2 Measurement of In-Plane Shear Kinematics

The in-plane shear kinematics occurring during the UBE test is an important measure as it can be used to estimate the in-plane bending stiffness of the sheared carbon fabric (see Section 5.5). The in-plane shear kinematics were measured (shown as data points in Figure 6) for both the untreated and treated carbon fabrics. Figure 6(a-c) are from the untreated fabric, Figures 6(d-f) are from the treated fabric. Again, the measured shear angle was taken directly from video footage of the test using Imagej (Ferreira and Rasband, 2012) while the ideal shear angle was calculated using the cross-head displacement and Eq (2). Figure 6 shows that at low shear angles, the measured angle at the centre of Region A is greater than the ideal angle for both untreated and treated fabrics. This excessive shear deformation at the centre of the sample compensates for the reduced shear deformation occurring at the top and bottom corners of Region A (which in turn is due to the fabric's resistance to sudden changes in fibre direction). In other words, because the top and bottom corners of Region A have a lower shear angle than the ideal theoretical prediction, then the centre has to shear more than the ideal prediction in order to accommodate the displacement imposed by the test machine, across the length of the UBE sample. Similar observations were discussed in

Ferretti et al., (2014) and were attributed to the influence of second gradient effects. The magnitude of this effect increases with decreasing specimen size, with the largest specimens (200x400mm) most closely following ideal shear kinematics (see Figures 6c and 6f). For the smallest specimens (100x200mm), the measured shear angle is up to 33% higher (i.e. 40^{o} rather than 30^{o}) than predicted by ideal shear kinematics (see Figure 6a and 6d). At higher shear angles, greater than 40^{o}, the experimentally measured shear angle begins to converge towards the theoretical shear angle. Ultimately, at shear angles greater than around 60^{o}, intra-ply slip means that the measured shear angle falls below the ideal angle. It should be noted that if the specimen size is cut too small then the specimen begins to lose integrity/cohesion very early in the test, intra-ply slip becomes problematic and the measured kinematics no longer lie above the ideal shear angle prediction (preventing identification of the fabric's in-plane bending stiffness). The optimum smallest sample size for the purpose of identifying the in-plane bending stiffness is found through trial and error and depends to a large extent on the ratio between the (specimen size)/(tow width), together with the fabric architecture. The results of Figure 6 suggest that the in-plane shear kinematics are insensitive to the DIC treatment. The red lines and blue dotted line in Figure 6 are predictions from simulations of the UBE test and are discussed further in Section 5.5.

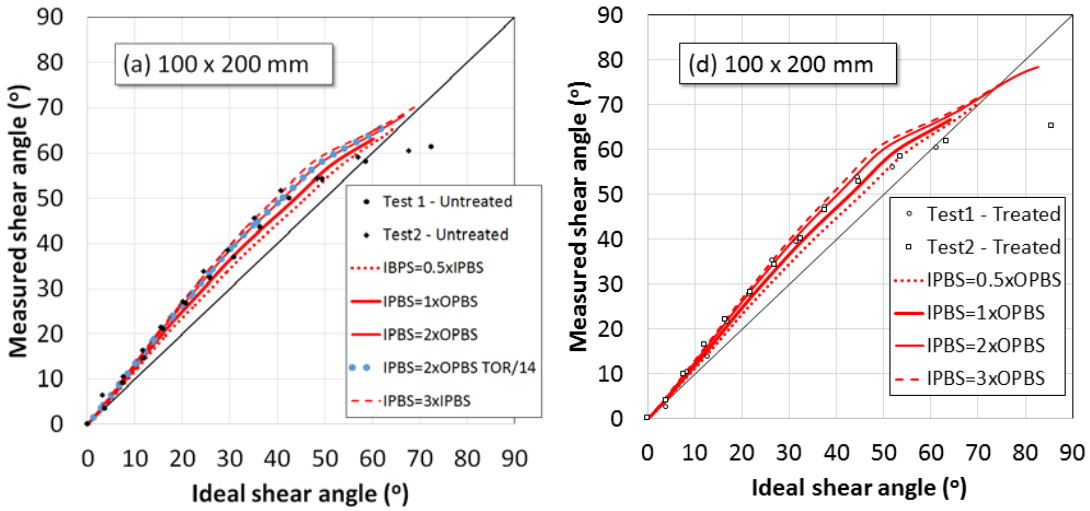

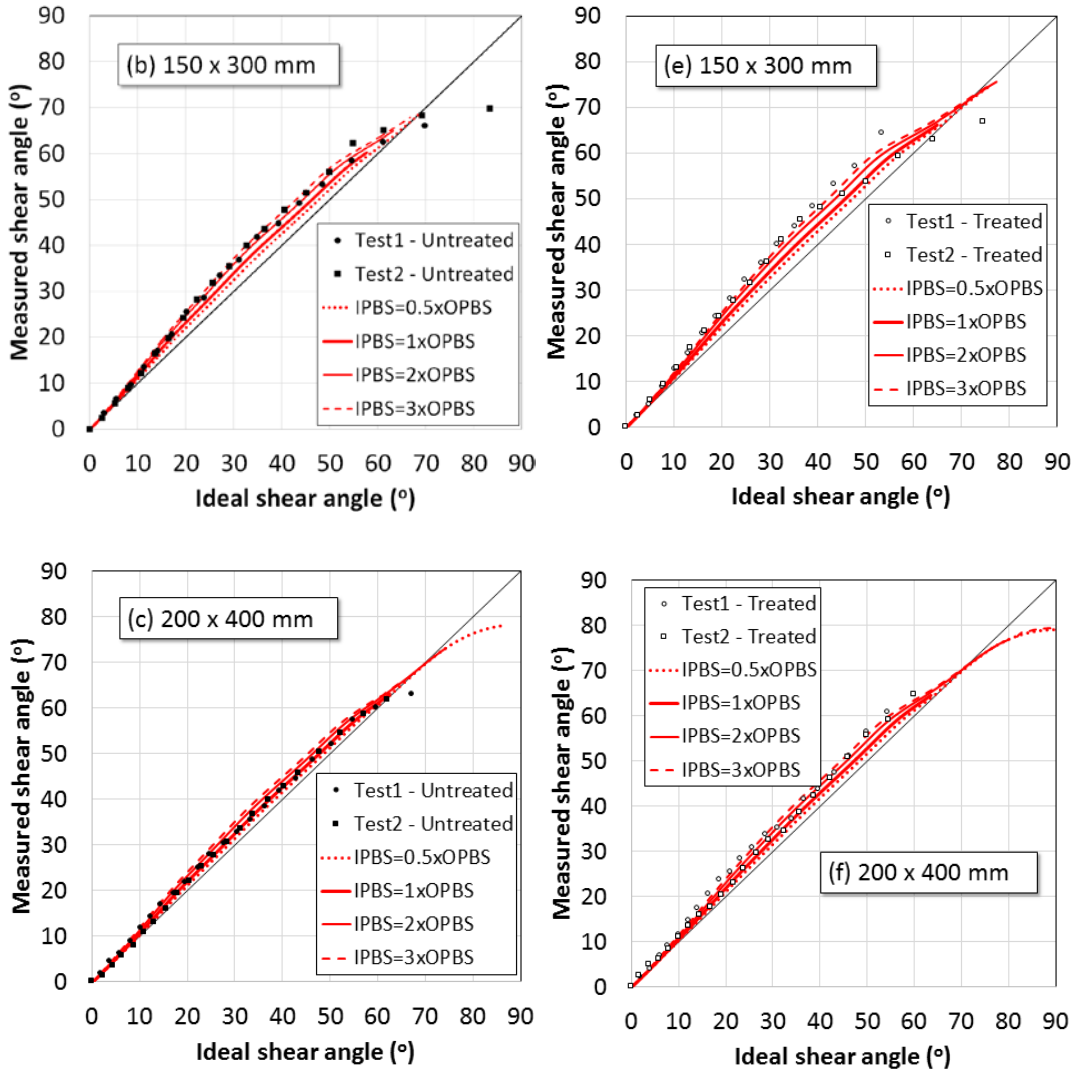

Figure 6. In-plane shear kinematics measured during UBE test for different sized samples (a-c) untreated carbon fabric (d-f) treated carbon fabric. The red lines are from simulations. In the legend IPBS is the in-plane bending stiffness per unit width, OPBS is the out-of-plane bending stiffness per unit width and TOR represents the modification factor of the default torsional stiffness per unit width.

3.4.3 Measurement of Wrinkle Onset Angle (Experimental), θ_{we}

The experimental wrinkle onset angle, θ_{we}, measured during UBE tests is an important measurement as it can be used to estimate the torsional stiffness of the sheared carbon fabric (see Section 5.6). Various methods of measuring the experimental wrinkle onset angle are possible, for example, use of back-light illumination, via analysis of tracking lines marked on the specimen (Harrison et al., 2012), though the use of the 'shape from focus' technique (Arnold et al., 2016) or via the use of a variety of commercially available non-contact 3-d

scanning methods, e.g. (Rashidi and Milani, 2016). In this investigation, out-of-plane wrinkling was identified using: (a) multiple video cameras positioned to provide clear views of the onset of wrinkling across the untreated fabric specimens and (b) via DIC (see Section 2.1). Measurement of the approximate values of θ_{we} for both the untreated and treated carbon fabrics revealed a reduction in θ_{we} with increasing specimen size (see yellow data points in Figure 7a and 7b). An important point to note is that the wrinkle onset angle of the treated specimen is significantly higher (by about 10^{o}) than that of the untreated specimen, despite the use of a relatively non-invasive treatment method for the DIC preparation (see Section 2.1). The blue and red lines in Figure 7 are predictions from simulations of the UBE test and are discussed further in Section 5.6.2. The generation of wrinkles is a gradual process and identifying θ_{we} is a currently a slightly subjective measurement partly based on human judgement. In order to reduce this subjectivity, DIC was also employed to monitor to the growth of the wrinkles.

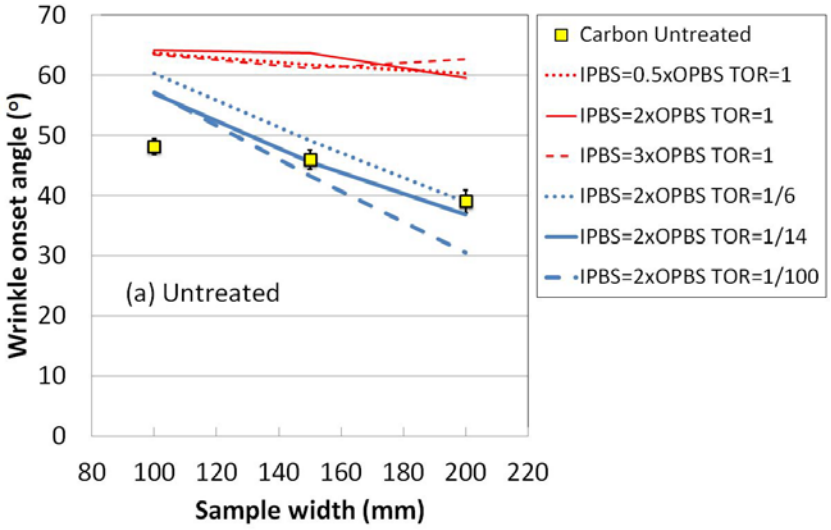

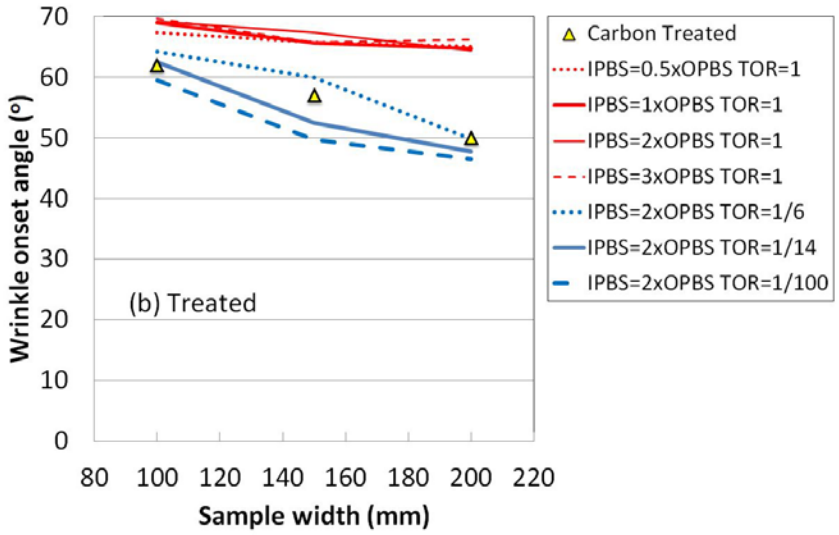

Figure 7. Wrinkle onset angle versus sample width. (a) Untreated carbon and (b) treated carbon. Experimental data given by yellow data points. Red and blue lines represent predictions from UBE test simulations (see Section 5.6.2). In the legend IPBS is the in-plane bending stiffness per unit width, OPBS is the out-of-plane bending stiffness per unit width and TOR represents the modification factor of the default torsional stiffness per unit width.

3.4.4 Out-of-Plane Displacement and Wrinkling Measured Using DIC

Tests on the treated carbon fabric were conducted while using the DIC technique (see Figure 8). The aim is to monitor the wrinkling behaviour of the fabrics during UBE tests.

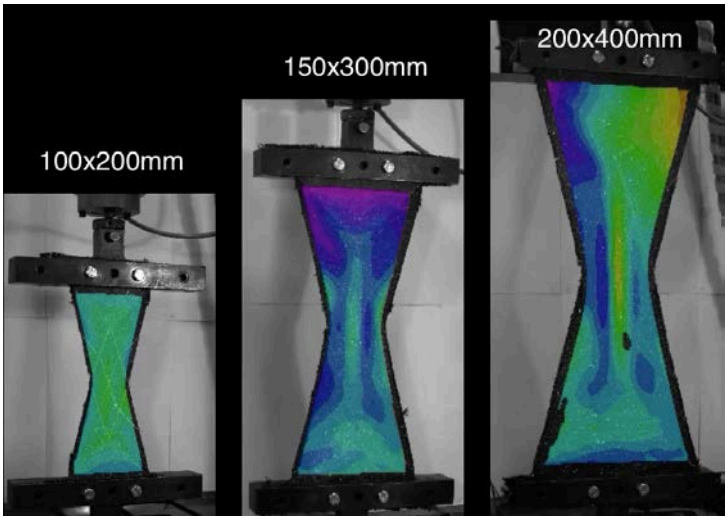

Figure 8. DIC measurements of out-of-plane displacement for 3 different specimen sizes. The same clamps were used in all tests. The actual specimens are discernible through the translucent colour map – see Figures 9-11 for the colour map scale.

After suitable sample treatment (see Section 2.1), DIC provides the possibility of monitoring the development of out-of-plane wrinkles more accurately than via simple visual analysis. Example results are shown in Figures 8 to 11. The measured shear angle at the centre of Region A is indicated in each image of Figures 9 to 11. Some of the specimens are not co-planar with the calibration plane of the DIC system and an initial out-of-plane twist is evident for the largest specimen due to an unintended rotation of the upper clamp. Nevertheless, the measurement of interest is the out-of-plane buckling of the specimen during shear. This measure can be readily extracted using the DIC software; the curved black lines marked across Figures 9 to 11 indicate the out-of-plane displacement across the mid-section of the specimens. The amplitude of the displacement uses the same scale as the scale-bar indicated in each figure. The advantage of DIC is that the form of the wrinkle can be accurately visualised, the disadvantage is that the treatment method, i.e. application of a speckle pattern, changes the mechanical response of the fabric, as reported in Section 3.4.2. As with the untreated carbon fabric, an increasing tendency to wrinkle with increasing sample size was observed. The smallest specimen size (100 x 200 mm) remained relatively flat until shear angles greater than 62^{o} (see Figure 9), the medium size specimen (150 x 300 mm) began wrinkling at around 57^{o} (see Figure 10) while the largest specimen (200 x 400 mm) began wrinkling at around 50^{o} (see Figure 11). These wrinkle onset values are compiled in Figure 7b and indicate a decrease in the value of θ_{we} with sample size but an increase in θ_{we} relative to the untreated carbon fabric (compare Figure 7a and 7b).

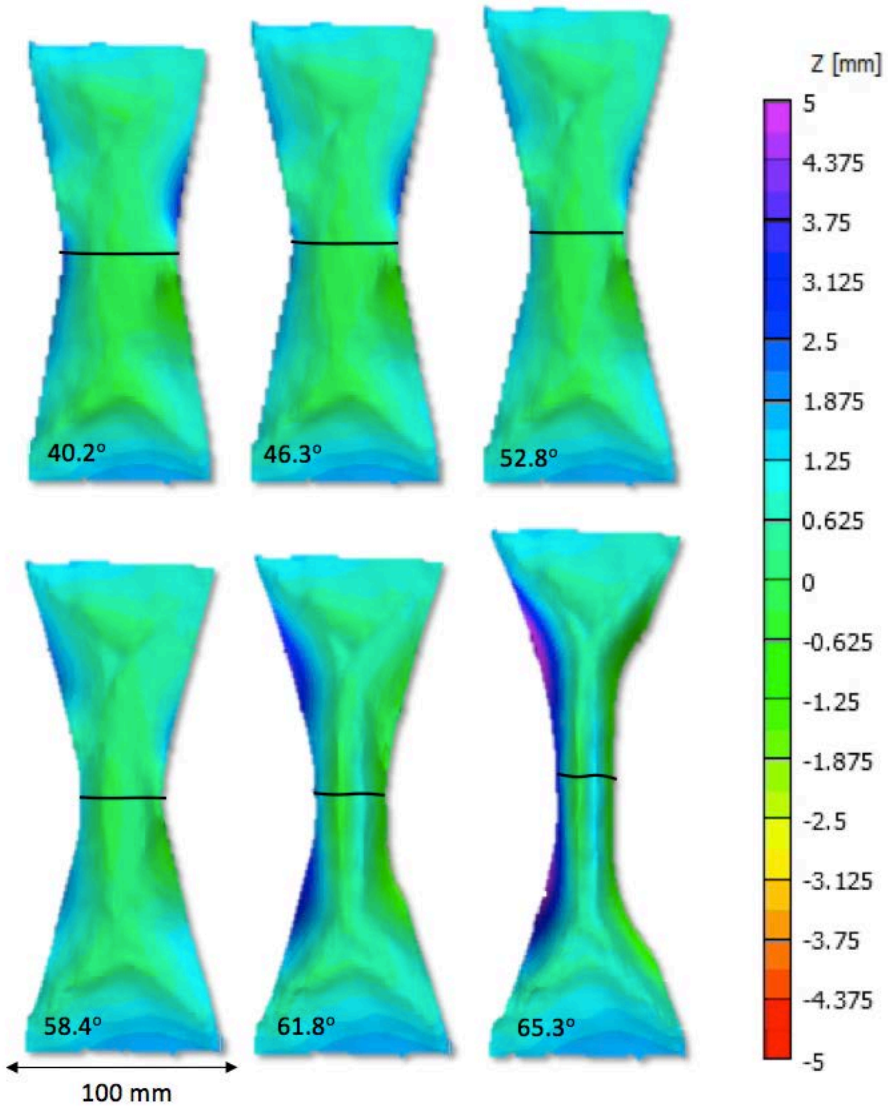

Figure 9. DIC measurements of the out of plane displacement across the surface of the 100 x 200 mm carbon fabric specimen. The black line indicates the out-of-plane displacement across the mid-section of the specimen.

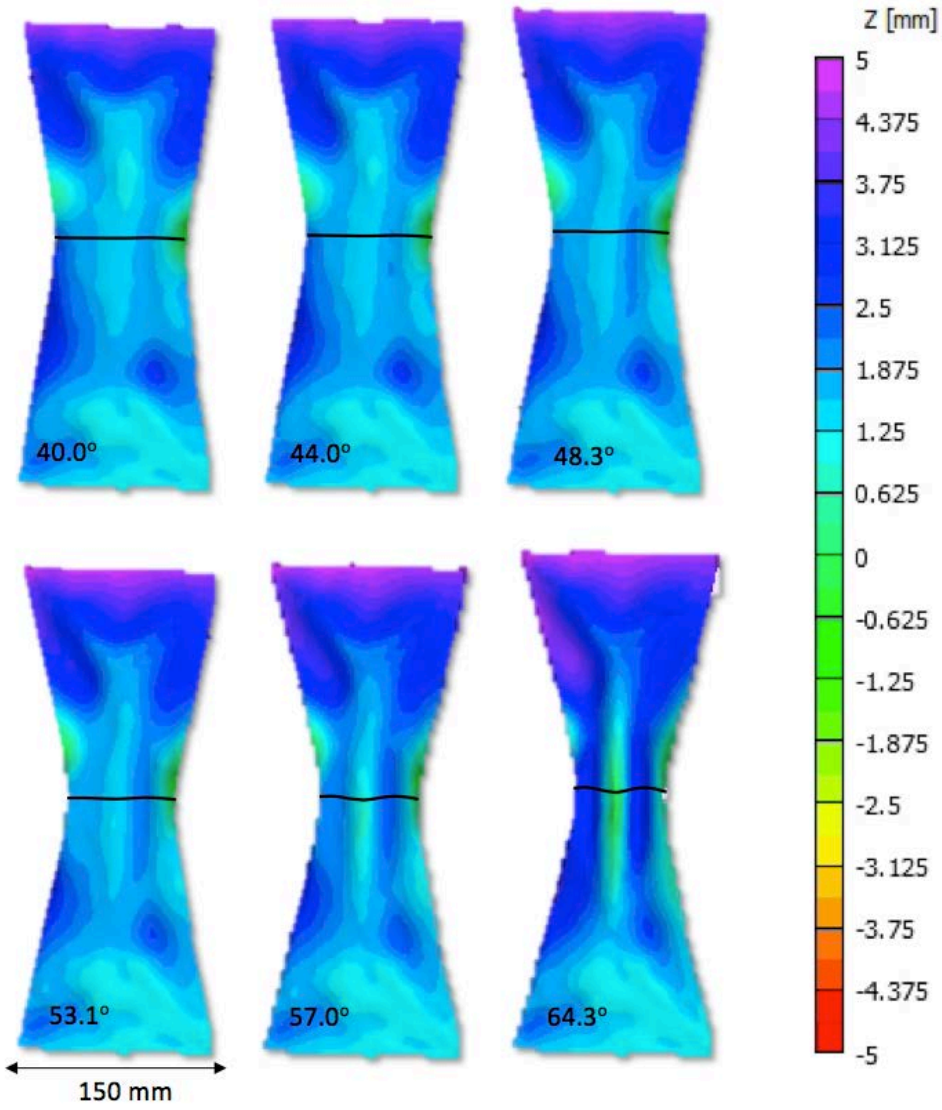

Figure 10. DIC measurements of the out of plane displacement across the surface of the 150 x 300 mm carbon fabric specimen. The black line indicates the out-of-plane displacement across the mid-section of the specimen.

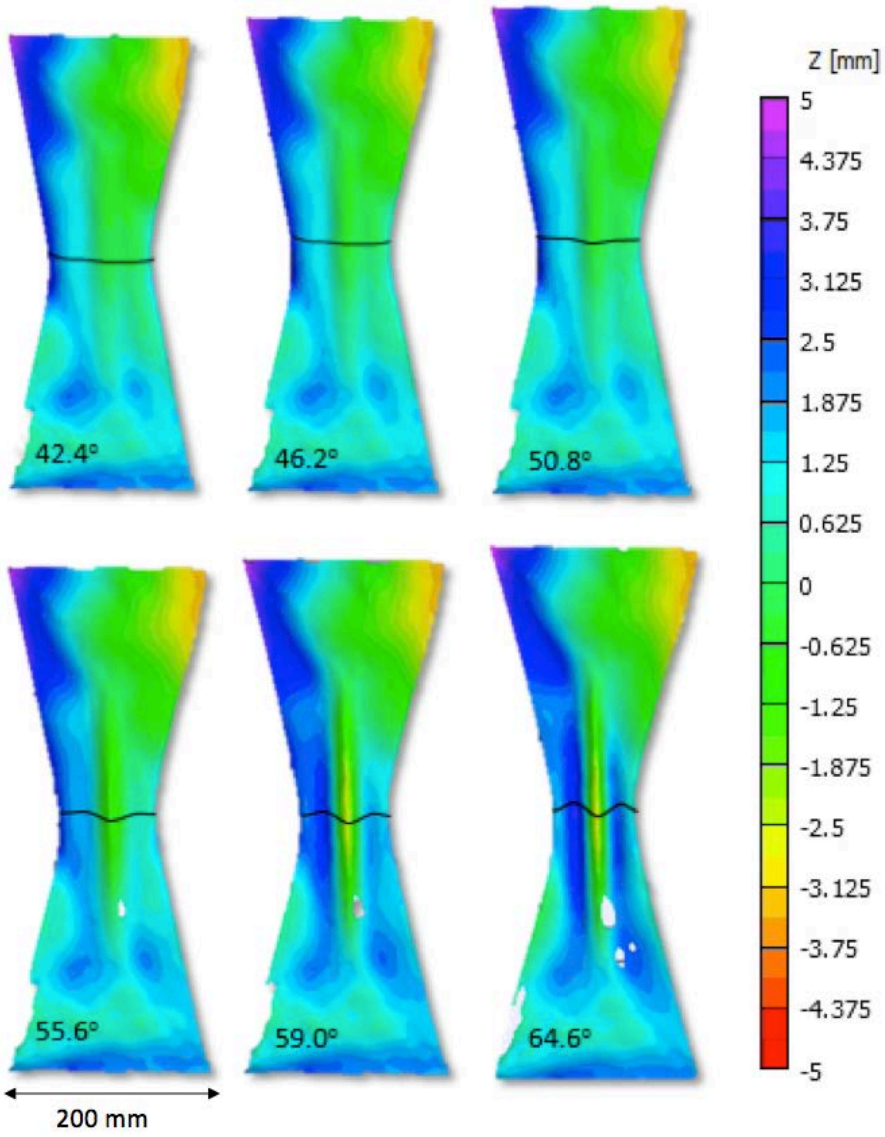

Figure 11. DIC measurements of the out of plane displacement across the surface of the 150 x 300 mm carbon fabric specimen. The black line indicates the out-of-plane displacement across the mid-section of the specimen.

4 Numerical Modelling

The test results presented in Section 3 can be used to directly measure several mechanical properties including out-of-plane bending in the two fibre directions and the shear stiffness of the fabric. In addition, given a sufficiently comprehensive forming model, several indirect measurements can be made via inverse modelling, including estimates of the torsional stiffness of both the un-sheared and sheared fabric and the in-plane bending stiffness of the fabric during shear. The modelling approach used in this investigation is briefly explained

below and the homogenisation theory originally presented in (Harrison, 2016) is extended to also consider torsional stiffness. After this, inverse modelling of the experimental results is conducted to estimate all remaining non-directly measurable mechanical properties.

4.1 Mutually Constrained Pantographic Beam and Membrane Mesh

Finite element simulations using a 'mutually constrained pantographic beam and membrane mesh' (Harrison, 2016) implemented in Abaqus Explicit™, have been conducted. The mesh is comprised of beam elements of length, *l*, and of rectangular cross-section with thickness, t_i, and width, w_i, where the subscript *i* equals 1 (warp) or 2 (weft), and square membrane elements, also of side length, *l*, connected via hinge elements (see Figure 12).

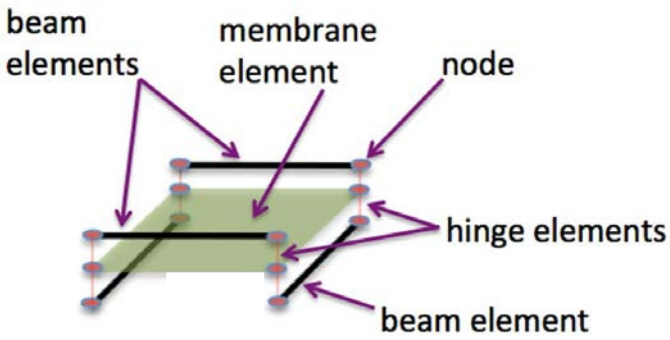

Figure 12. Repeat unit cell structure of the mutually constrained pantographic beam and membrane mesh, image from reproduced from Harrison (2016).

This mesh structure means that the elements translate together (mutually constrained) while permitting torque-free rotation of the two, initially perpendicular sets of beam elements, similar to a pantograph (D'Agostino et al., 2015; Giorgio, 2016). Homogenisation theory relating the macro-scale tensile and flexural properties of the fabric, to the properties (physical density, stiffness and cross-section) of the structural elements within the mesh was presented in (Harrison, 2016). The goal of the homogenisation theory was to allow the macro-scale mechanical properties of the sheet to be independently set, and to dissociate these properties from the element length within the mesh (i.e. the mesh density). To achieve this, the beam stiffness, E_i and the beam cross-section (thickness, t_i and width, w_i) were related to the tensile line-stiffness per unit width, γ (Sharma and Sutcliffe, 2004), the out-of-plane bending stiffness per unit width, β, the in-plane bending stiffness per unit width, α, the specimen/blank width, *W*, and the beam element length, *l*, as

$$E_i = \frac{\gamma_i^2 W l}{12(W+l)\sqrt{\alpha_i \beta_i}} \quad (4)$$

$$t_i = \sqrt{\frac{12\beta_i}{\gamma_i}} \quad (5)$$

$$w_i = \sqrt{\frac{12\alpha_i}{\gamma_i}} \quad (6)$$

where the subscript, *i*, indicates the orientation of the set of beam elements, in either the 1 (warp) or the 2 (weft) direction. The fabric's shear stiffness is modelled using the so-called 'stress-power model' implemented in the membrane elements (Harrison et al., 2011) and relationships between the density of the beam and membrane elements to the areal density of the fabric are also provided in Harrison (2016). A notable omission in the homogenisation theory presented in Harrison (2016) relates to the sheet's torsional stiffness. The latter is known to play an important role in textile mechanics (Cooper, 1960; Hu, 2004; Lomov and Verpoest, 2006; Steigmann and Dell'Isola, 2015) and is shown in this investigation to have an important influence on wrinkling behaviour during shear. It is therefore essential to understand how the torsional stiffness of the beam elements within the mutually constrained pantographic beam and membrane mesh can be calculated such that the macro-scale torsional stiffness of the sheet is also dissociated from the element length within the mesh. The underlying assumption used in this investigation is that if each tow has a measurable torsional stiffness (Lomov et al., 2003), then a fabric composed of an array of such tows must also possess a torsional stiffness.

4.2 Homogenisation of Torsional Stiffness

Timoshenko beam elements (type B31) are employed and use of a general beam section in Abaqus Explicit™ permits independent control over both the transverse shear stiffness and the torsional stiffness of the beam elements in the mesh. Throughout this investigation, the transverse shear stiffness is maintained at the default value calculated by Abaqus (User's Manual 6.14), this means that the Timoshenko beam elements provide a close approximation to the Euler-Bernoulli theory of bending beams (Philpot, 2011). According to established beam theory (Philpot, 2011) the torque generated due to the twisting of an elastic beam is given as

$$T = \Gamma a^3 b G_t \left(\frac{\Psi}{L_b}\right) \quad (7)$$

where $\Gamma(b/a)$ is a dimensionless numerical constant given by St Vernant's analysis of the torsion of rectangular beams and depends on the aspect ratio between the short and long side lengths of the cross section of the beam (given here as *a* and *b* respectfully), ψ (rads) is the angular twist at the end of the beam, L_b (m) is the length of the beam (not to be confused with the length of the individual beam elements) and G_t (Nm^{-2}) is the torsional shear rigidity of the beam. For the mutually constrained pantographic beam and membrane mesh, the torsional stiffness per unit width of the sheet along the warp and weft directions is simply the sum of the torsional stiffness of each of the individual beam elements per unit width of the mesh. Thus,

$$T_i = \Gamma_i a_i^3 b_i G_{ti} \left(\frac{\psi_i}{L_{bi}}\right) \left\{\frac{W+l}{Wl}\right\} \tag{8}$$

Because the Poisson's ratio of all beam elements in this investigation is chosen to be zero, $G_{ti} = E_i/2$ where E_i is the Young's modulus of the beam elements orientated in the *i* direction and is given by Eq (4). Substituting Eq (4) in Eq (8) gives

$$T_i = \Gamma_i a_i^3 b_i \frac{\gamma_1^2}{24\sqrt{\alpha_1\beta_1}} \left(\frac{\psi_i}{L_{bi}}\right) \tag{9}$$

The main point to note in Eq (9) is that dependence of the torsion per unit width, T_i, on the element length, *l*, is eliminated. Assuming, $\beta_i < \alpha_i$ (later experimental evidence will show this is the case for the carbon fabric under consideration), then , $w_i > t_i$ and so $a_i = t_i$ and $b_i = w_i$. Thus, using these equalities and substituting Eq (5) and (6) in Eq (9) find,

$$T_i = 3\Gamma\beta_i \left(\frac{\psi_i}{L_{bi}}\right) \tag{10}$$

and also using Eq (5) and (6),

$$\frac{b_i}{a_i} = \frac{w_i}{t_i} = \sqrt{\frac{\alpha_i}{\beta_i}} \tag{11}$$

it becomes apparent that since $\Gamma_i(b_i/a_i)$ or, using Eq (11), $\Gamma_i\left(\sqrt{\alpha_i/\beta_i}\right)$, then the torsional stiffness per unit width in a given fibre direction, is purely a function of the in-plane and out-of-plane bending stiffness, α and β (note that if $\alpha_i < \beta_i$ then Eq (11) simply becomes $T_i = 3\Gamma_i\alpha_i(\psi_i/L_{bi})$). Thus, the torsional stiffness can be controlled, while maintaining

independence from the element length, simply by introducing a dimensionless parameter, ξ_i, such that

$$T_i = 3\frac{\Gamma_i}{\xi_i}\beta_i\left(\frac{\psi_i}{L_{bi}}\right) \quad (12)$$

The torsional stiffness per unit width in each fibre direction can thus be written as

$$\mu_i = 3\frac{\Gamma_i}{\xi_i}\beta_i \quad (13)$$

when $\beta_i < \alpha_i$ (or $\mu_i = 3\frac{\Gamma_i}{\xi_i}\alpha_i$ when $\alpha_i < \beta_i$). Validation of this theory is discussed in Section 5.3.

5 Determination of Numerical Model Parameters

In this section, the process of determining all the required mechanical properties for the numerical model, mainly from the experimental data presented in Section 3, is demonstrated.

5.1 Determination of Tensile Stiffness

Measurement of the true tensile properties of the carbon fabric is considered unnecessary for the purpose of this investigation for reasons relating to necessary approximations used the simulation approach. Simulation time can be a problematic issue when conducting dynamic explicit finite element simulations due to the large number of time increments required in reaching the total step time. If material damping is ignored, a non-conservative estimate of the maximum stable time increment, Δt, calculated on an element-by-element basis for isotropic linear elastic material behaviour with a Poisson's ratio of 0, is given by,

$$\Delta t = L_e\sqrt{\frac{\rho_e}{E_e}} \quad (14)$$

where L_e is the characteristic length of elements in the mesh, ρ_e is the material density assigned to the element and E_e is the modulus of the material assigned to the element (see Section 6.3.3 of the Abaqus User's Manual 6.14). Consequently, for a given mesh density, faster simulations can be run by maximising the ratio ρ_e/E_e via mass-scaling, or by decreasing the total time step time using velocity scaling. However, both these options

introduce the risk of potentially undesirable inertial effects that can change wrinkling predictions (see Section 5.6.1). For this reason, mass scaling is avoided in this investigation and the use of velocity scaling is limited. Instead, in order to reduce simulation time, the tensile properties of the model in each of the two fibre directions are significantly reduced from their true value (i.e. > 100GPa). This is permissible only as long as this change in material property has negligible influence on the forming predictions. Due to the relatively low tensile forces imposed during the experimental tests, a tensile modulus of 3 GPa (or equivalently, a line stiffness per metre, γ_i, of 600 KNm^{-1}) is low enough to keep simulation times to manageable levels but still high enough to limit localised tensile strains to less than 1% in the UBE test simulations; a level of strain typically measured in woven engineering fabrics due to un-crimping and compaction of the woven fabric when subject to tensile loads (Boisse et al., 2001; Potluri and Thammandra, 2007); discussion of the effect of this reduction in the fibre tensile modulus on kinematic predictions is provided in Section 5.5. The linear tensile stiffness ignores the initial non-linear tensile response of woven fabrics due to fabric crimp and is a limitation of the modelling approach. The same tensile stiffness value was used in all simulations of this investigation.

5.2 Determination of Out-of-Plane Bending Stiffness

The out-of-plane bending stiffness in the two fibre directions is simple to measure and is taken directly from the values determined by the cantilever tests conducted using samples cut in the warp and weft directions. The ability of the modelling approach (Section 4) to accurately model the bending stiffness of the fabric when tested along the fibre direction was verified in Harrison (2016) and is omitted here. The values used in the simulations are given in Table 1 and are simply the average values shown in Figure 2.

Table 1. Out-of-plane bending stiffness per unit width, β_i, used in all simulations.

	Warp Direction (Nm)	Weft Direction (Nm)
Untreated Carbon Fabric	$\beta_1 = 0.00023$	$\beta_2 = 0.00018$
Treated Carbon Fabric	$\beta_1 = 0.00030$	$\beta_2 = 0.00024$

5.3 Determination of Shear Stiffness

The shear force per unit length versus shear angle behaviour required by the stress power model (Harrison et al., 2011) implemented in the membrane elements of the mutually constrained pantographic beam and membrane mesh (Harrison, 2016), is determined by normalising the axial force versus shear angle data shown in Figure 5, using Eq (3). The normalisation theory behind Eq (3) includes the assumption of ideal shear kinematics across the UBE test specimen. As discussed in Section 3.4.3, Figure 6 suggests the largest specimens (200x400mm) most closely follow ideal shear kinematics, for this reason the data shown in Figure 5c (untreated fabric) and Figure 5f (treated fabric) were used to find the shear force per unit length versus shear angle behaviour for the untreated and treated fabric. This resulted in two different 9th order polynomials, the coefficients of which are provided in Table 2.

Table 2. Coefficients of 9th order shear force versus shear angle polynomial input curves used for Untreated and Treated Carbon Fabrics.

Untreated Carbon Fabric	Treated Carbon Fabric
$F_{sh}(\theta) =$	$F_{sh}(\theta) =$
0.1507010016075160θ	0.5925757520204930θ
$-0.0341632443681710\theta^2$	$-0.1415885646262640\theta^2$
$+0.0060487703731360\theta^3$	$+0.0199838285268260\theta^3$
$-0.0006182215787200\theta^4$	$-0.0015934655542910\theta^4$
$+0.0000358846026830\theta^5$	$+0.0000746341964490\theta^5$
$-0.0000012010848250\theta^6$	$-0.0000021000825430\theta^6$
$+0.0000000229847080\theta^7$	$+0.0000000349486130\theta^7$
$-0.0000000002334040\theta^8$	$-0.0000000003167530\theta^8$
$+0.0000000000009750\theta^9$	$+0.0000000000012040\theta^9$

It is important to understand the sensitivity of the axial force prediction to changes in the in-plane bending stiffness and the torsional stiffness used in the model. To this end, two sensitivity studies were conducted with the tensile line stiffness per unit width fixed at 600KNm^{-1}, the out-of-plane bending stiffness per unit width in each fibre direction, β_i, set to the values shown in Table 1 and the shear force per unit length, $F_{sh}(\theta)$, determined using the polynomials of Table 2. In the first study, the torsional stiffness per unit width in each fibre

direction, μ_i, see Eq (13), was initially set with $\xi_i = 1$ (resulting in a relatively high torsional stiffness) and the in-plane bending stiffness per unit width in each fibre direction was varied such that $\alpha_h = 0.5\beta_h, \beta_h, 2\beta_h$ & $3\beta_h$ where β_h is the higher of the two measured values (see Table 1), the resulting force predictions are indicated by the red lines in Figure 5, which are closely superposed. Next the in-plane bending stiffness per unit width in each fibre direction was held fixed at $\alpha_i = 2\beta_1$ and the torsional stiffness per unit width in each fibre direction was varied such that, $\xi_i = 6$, 14 & 100. As with the predictions produced using different values of α_h (the red lines), predictions produced using the three different values of ξ_i, all fall on almost exactly the same line and so just one example axial force prediction is presented in Figure 5, indicated by the dotted blue line in Figure 5a (here $\xi_i = 14$). Axial force predictions from the simulations (both red lines and dotted blue line) are very close to the experimental data, especially for the 200x400mm specimen size (to be expected given that this data was used to determine the polynomial coefficients given in Table 3). The predictions demonstrate the accuracy of the shear part of the model (Harrison et al., 2011) and close superposition of all the axial force predictions indicate a lack of sensitivity of the axial force prediction to the values of either the in-plane bending stiffness or the torsional stiffness used in the model. This implies that the shear stiffness can be accurately determined from the axial force, irrespective of the values of the in-plane bending stiffness or the torsional stiffness used in the simulations.

5.4 Determination of Torsional Stiffness (of un-sheared fabric)

The torsional stiffness of the un-sheared fabric can, in principal, be estimated by both theoretical and numerical means from the results of the cantilever bending tests. For completeness, both approaches are discussed here though it will be shown that, at least for the fabric under consideration, the numerical method is more reliable than the theoretical approach.

5.4.1 Determination of Torsional Stiffness Estimated via Theoretical Analysis

Several theoretical analyses of the bending properties of fabrics have been published and consider not just the bending stiffness of the fabric in the fibre directions but also the fabric's torsional stiffness (Hu, 2004). Note that torsional stiffness has no influence when measuring the bending stiffness of the un-sheared fabric in the two fibre directions but has a significant effect when measuring the bending stiffness in an off-axis direction (e.g. 45^o).

Here both sets of tows within the fabric are subject to twist. The theoretical analysis of the cantilever bending test (see Section 3.1) developed by Cooper (1960) considers both bend and twist (in the absence of fabric shear) and is simple to apply, for this reason the theory is recommended by Hu (2004) and is employed here. By measuring the bending stiffness in the warp, weft and off-axis directions (e.g. in the 45^o direction), a theoretical estimate of the torsional rigidity of a fabric can be obtained. The pertinent equation from this theory, as presented by Hu (2004) is

$$J_1 + J_2 = 4\beta_{45} - (\beta_1 + \beta_2) \quad (15)$$

where the subscripts, 1 and 2 and 45 indicate the parameter is associated with the fabric specimens orientated with their longer dimension in the 1 (or warp), 2 (or weft) and 45^o (bias) directions. $(J_1 + J_2)$ is a measure of the torsional rigidity of the fabric per unit width and β_1, β_2 and β_{bias} are the out-of-plane bending rigidities per unit width in the warp, weft and bias (45^o) directions. β_1, β_2 and β_{45} can be found using Eq (1) by testing samples cut along the three different directions. Theoretically, the three values of β_i, for both the untreated and treated carbon fabric, can be substituted in Eq (15) to obtain an estimate of the torsional stiffness per unit width of the sheet before and after treatment for DIC analysis. Following this procedure, the value of $(J_1 + J_2)$ for the untreated fabric is found to be -0.000098 Nm while the value for the treated fabric is found to be -0.000174 Nm. Clearly, these negative predictions are impossibly low. Reasons for this error are probably related to the assumptions of the theory; the fabric has no internal slip mechanisms (the difference in results from bending tests in the bias direction using the 20mm and 100mm wide samples suggests intra-ply slip does occur – see Figure 3) and the theory also assumes zero fabric shear due to gravity. The action of both these mechanisms tends to reduce the measured bending stiffness of the fabric. Because the bending stiffness in the two fibre directions in Eq (15) are considered constant, with no other mechanisms considered within the theory other than torsional stiffness, the stiffness-reduction mechanisms (slip and shear) are simply attributed to a lower value of the torsional stiffness for the fabric, resulting in negative predictions. A better interpretation of this result is that some degree of intra-fabric slip and fabric shear probably occurs during the bending test and that the torsional stiffness of the fabric is very low; though no accurate value can be determined using this theoretical

approach with this particular fabric (the theory is more effectively used with regular, non-engineering fabrics (Cooper, 1960)).

5.4.2 Determination of Torsional Stiffness Estimated via Inverse Numerical Analysis

As discussed in Section 5.3.1, the torsional stiffness of the beam elements influences the out-of-plane bending stiffness of the cantilever specimen when the sample is cut with its long axis along the bias direction. Simulations were conducted in order to match the numerical results with the experimentally measured bending stiffness found in the bias direction for both the untreated and treated carbon fabric. To do this the tensile line stiffness per unit width in each fibre direction was fixed at 600KNm^{-1}, the out-of-plane bending stiffness per unit width in each fibre direction, β_i, was set to the values shown in Table 1 and the shear force per unit length, $\mathrm{F_{sh}}(\theta)$, was determined using the polynomials of Table 2. The in-plane bending stiffness, α_i, was set as $2 \times \beta_i$ (a value shown to be reasonable in Section 5.5). By changing ξ_i in Eq (13) (while maintaining $\xi_1 = \xi_2$), the torsional stiffness per unit width of the sheet was varied until the bend angle of the specimen, ϕ, indicated a bending stiffness to within 1.5% of the experimentally measured values. Rayleigh damping with a coefficient of 30 s^{-1} was used to prevent oscillations of the cantilever specimen in the simulations. For convenience, the same mesh for the cantilever specimen, measuring 0.098 x 0.021m, was used throughout this exercise and the bending stiffness was determined from the predicted value of ϕ, the areal weight of the fabric, p, and the overhang length of the specimen, L_s using the empirically determined formula (Harrison, 2016)

$$\beta_i = \frac{f(\phi)}{\frac{\tan\phi}{\cos(0.5\phi)}} \times \frac{pL_s^3}{8} \qquad (16)$$

where

$$f(\phi) = (-3.2434387343 \times 10^{-5}) \cdot \phi^2 + (3.8717591439 \times 10^{-6}) \cdot \phi + 0.9988589066$$

Note that, ϕ, is expressed in degrees in just the polynomial function and in radians in the trigonometrical function of Eq (16). This correction to Eq (1) is required whenever the bend angle is not equal to that specified in the British Standard, i.e. 41.5^{o}. A simulation of a

cantilever test sample with the in-plane fibre directions orientated at 45° to the long axis of the specimen (i.e. in the bias direction), and assigned the measured mechanical properties of the untreated fabric is shown in Figure 13. Values of the torsional stiffness per unit width of the fabric approximated using inverse modelling are provided in Table 3 and indicate that the torsional stiffness of the fabric is very low; around 4% of the out-of-plane bending stiffness of the fabric ($\xi_i = 14$). A small degree of shear is apparent in the specimen, explaining the discrepancy between the theoretical prediction of Section 5.4.1 and this numerical prediction. Use of the homogenisation theory presented in (Harrison, 2016) and Section 4.2 means that these numerical predictions should be independent of mesh density, a point that was verified by mesh sensitivity studies.

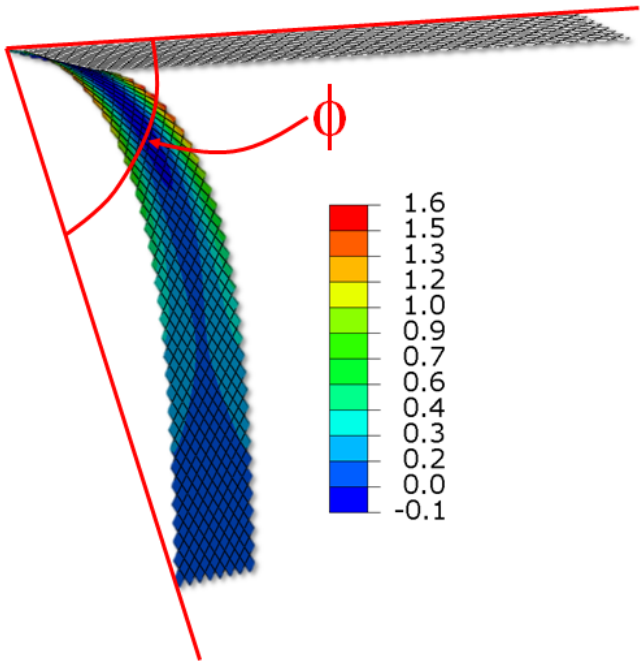

Figure 13. Cantilever bend test in bias direction showing specimen before and after bending. The colour legend indicates shear angle of the specimen. The out-of-plane bend angle was adjusted to produce the same bending stiffness as the untreated carbon fabric, here $\phi = 66.2^0$.

Table 3. Torsional stiffness per unit width of un-sheared fabric estimated via inverse analysis of cantilever test performed in the bias (45°) direction.

	Warp Direction (Nm)	Weft Direction (Nm)
Untreated Carbon Fabric	$0.0404\beta_1 = 9.30 \times 10^{-6}$	$0.0438\beta_2 = 8.06 \times 10^{-6}$
Treated Carbon Fabric	$0.0404\beta_1 = 12.64 \times 10^{-6}$	$0.0424\beta_2 = 10.58 \times 10^{-6}$

5.5 Determination of the In-Plane Bending Stiffness

The in-plane bending stiffness per unit width, α_i, is estimated via inverse modelling. The strategy is to adjust α_i (here $\alpha_1 = \alpha_2$) used in simulations of the UBE test in order to reproduce the observed in-plane shear kinematics for the different sized specimens. To this end, the tensile line stiffness per unit width in each fibre direction was fixed at 600KNm^{-1}, the out-of-plane bending stiffness per unit width in each fibre direction, β_i, was set to the values shown in Table 1 and the shear force per unit length, $\mathrm{F_{sh}}(\theta)$, was determined using the polynomials of Table 2. The torsional stiffness per unit width in each fibre direction, μ_i, was initially set with $\xi_i = 1$ (resulting in a relatively high value of the torsional stiffness) and the in-plane bending stiffness was varied such that $\alpha_h = 0.5\beta_h, \beta_h, 2\beta_h$ & $3\beta_h$ where β_h is the higher of the two measured values of the out-of-plane bending stiffness (see Table 1). The resulting predictions of the shear angle at the centre of the specimen versus the ideal shear angle, using these different values of α_h and for each specimen size are presented in Figure 6 (the red lines) alongside the experimental data. The increasing sensitivity of the shear angle to changes in the in-plane bending stiffness, with decreasing specimen size, makes the smallest specimen size the best choice for determining in-plane bending stiffness. A good fit to the experimental data of Figure 6a (untreated fabric) and Figure 6d (treated fabric) was obtained, using a value of $\alpha_h = 2\beta_h$. This same value also produced a good fit to the data measured for the two larger specimen sizes adding confidence in this result (see Figures 6b, 6c, 6e & 6f). (Note that above 70^{o}, the numerically predicted shear angle eventually falls below the ideal shear angle. Unlike the experimental data which shows a similar effect due mainly to the occurrence of intra-ply slip, the fall in the numerical prediction is due to the occurrence of tensile strain along the fibre directions, as the shear stiffness becomes very large. Increasing the tensile modulus of the fibres tends to delay this effect to a small degree, at the cost of increasing simulation time). The predicted in-plane shear kinematics show a similar dependence on sample size as seen in the experimental data (i.e. converging towards ideal shear kinematics as the sample size increases). Figure 14 shows simulations of the three UBE specimen sizes (scale shown below each image). The in-plane full-field shear angle distribution is provided; each specimen is at the same relative displacement (d/L_A=0.34). All three specimens have identical mechanical properties but

their shear kinematics are visibly different. The simulations show a similar specimen size-dependent change in behaviour as the experimental data and is another way of illustrating the results presented in Figure 6. Again, use of the homogenisation theory presented in (Harrison, 2016) and Section 4.2 means that these numerical predictions should be independent of mesh density, a point verified by mesh sensitivity studies.

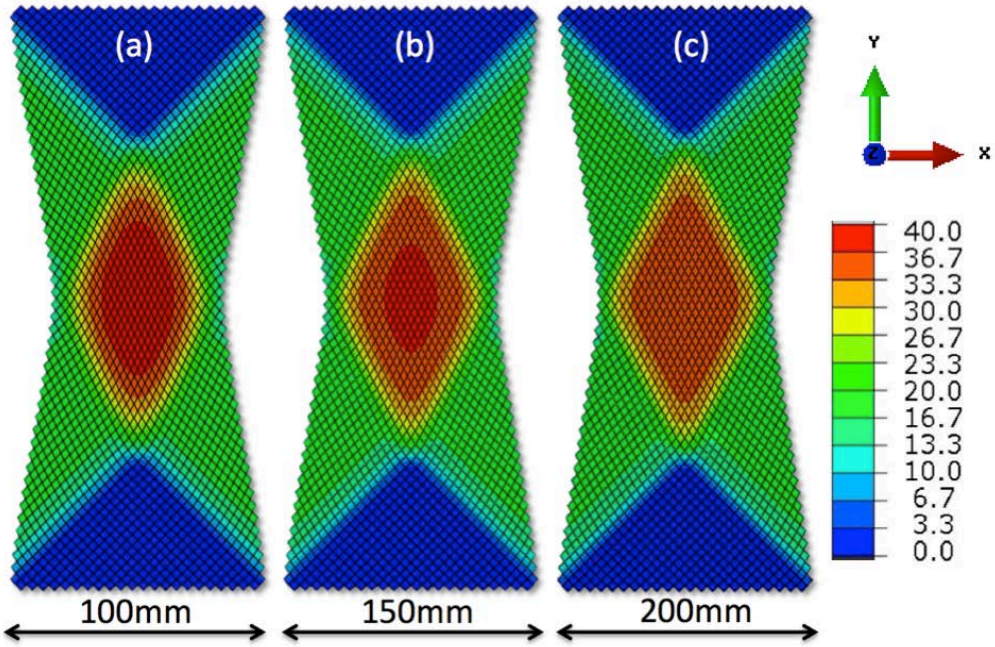

Figure 14. Full field shear angle distribution across different sized specimens. All specimens have identical homogenised macro-scale mechanical properties but undergo slightly different shear kinematics dependent on the specimen size. (a) 100x200mm, max shear angle = 40^{o}, (b) 150x300mm, max shear angle = 37.2^{o}, (c) 200x400mm, max shear angle = 35.5^{o}. The ideal shear angle for all 3 specimens is 30.9^{o}. The legend indicates the shear angle.

Once again, in order to use this in-plane stiffness fitting procedure, it is important to understand the sensitivity of the in-plane shear kinematics to changes in the torsional stiffness per unit width in each fibre direction of the sheet, μ_i. To this end, the in-plane bending stiffness per unit width in each fibre direction was held fixed at $\alpha_i = 2\beta_1$ and the torsional stiffness was varied such that, ξ_i =6, 14 and 100. Shear angle predictions produced using the three different values of ξ_i, all fall on almost exactly the same line and so just one example shear angle prediction is presented in Figure 6, indicated by the dotted blue line in Figure 6a (here $\xi_i = 14$). The results indicate that the in-plane shear kinematics

are insensitive to changes in the torsional stiffness, μ_i, of the fabric. This implies that the in-plane bending stiffness can be determined irrespective of the values of the torsional stiffness used in the simulations.

5.6 Determination of Torsional Stiffness (of sheared fabric)

For most woven engineering fabrics, given a sufficiently large UBE test specimen, an out-of-plane wrinkle appears as the sample reaches high shear angles. Invariably, in a well-aligned UBE test (using a relatively well-balanced woven engineering fabric), this wrinkle is vertically orientated along the long axis of the test specimen, see for example, Figures 8-10 in this paper, Figure 5 in (Harrison et al., 2012), Figure 7 in (Harrison, 2016)) or Figure 4 in Rashidi and Milani (2016). Tows running through this wrinkle undergo both out-of-plane bending and twisting kinematics as the wrinkle grows (similar to the manner in which obliquely orientated tows in a cantilever test specimen also undergo twist kinematics, see Section 5.3). The in-plane compressive stress acting across the width of the specimen is directly related to the shear stress of the fabric (Harrison et al., 2011). Thus, the onset of fabric wrinkling in a UBE test is governed by the interplay of the fabric's shear stress, which promotes wrinkling (and which is itself influenced by the affect that the in-plane bending stiffness has on the in-plane shear kinematics, see Figure 14) and its out-of-plane bending stiffness and torsional stiffness; both of which tend to suppress out-of-plane wrinkling. Consequently, all of these mechanical properties have to be accurately modelled if the experimental wrinkle onset angle, θ_{we}, is to be correctly predicted in UBE test simulations. Note that no initial perturbation is used to generate wrinkles in any of the UBE simulations, the wrinkles naturally grow from noise in the numerical solution.

5.6.1 Influence of Inertia on the Predicted Wrinkle Onset Angle, θ_{wp}

Prior to determining the torsional stiffness of the sheared specimen via inverse analysis it is important to understand if any other factors can influence the generation of wrinkles in the UBE test simulations. Preliminary simulations revealed that that θ_{wp} is extremely sensitive to inertia; increasing inertia increases θ_{wp}, ultimately suppressing wrinkling entirely. In the simulations of this investigation, θ_{wp} is defined as the shear angle at which the wrinkle amplitude across the mid-section of the specimen first exceeds 1mm. As discussed in Section 5.1, techniques to reduce simulation time when using the explicit finite element

method include artificially increasing simulation speed (normally valid for rate independent materials) and mass scaling; both can introduce inertial effects. By reducing inertia (or kinetic energy), while keeping the mechanical properties constant, values of θ_{wp} were found to tend towards a constant lower plateau value (see Figure 15), though when using realistic mechanical properties and areal densities, simulation times lasting several hundred hours are required to reach this plateau when using the mesh density shown in Figure 14 (computer specification: Intel Core i7-3770 CPU@3.40GHz; 32.0GB, 64-bit OS).

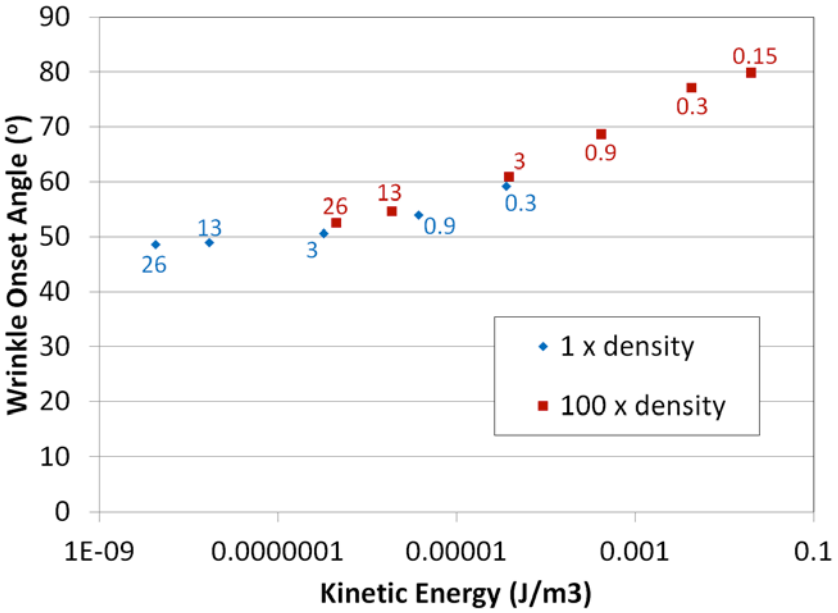

Figure 15. Kinetic energy per unit volume of sample just prior to wrinkling versus θ_{wp}. The macro-scale mechanical properties of each simulation were the same, only the simulation speed and areal density were changed. The numbers in the graph indicate the simulation time (step time) of each data point in seconds. A plateau value of the wrinkle onset angle is observed at very low kinetic energies.

As a compromise between accuracy and simulation time, the homogenised sheet density was chosen equal to the actual areal density of the carbon fabric (i.e. 1 x density) while the speed of the simulations was increased by a few times in comparison to actual experiments (e.g. 3 seconds rather than about 10 to 20 seconds per test, depending on specimen size). This resulted in θ_{wp} just one or two degrees higher than that found for the plateau value (for this particular set of mechanical properties the plateau occurs around 49° – see Figure 15), with simulation times of around 50 hours per simulation; slow but manageable. Again, use of the homogenisation theory presented in Harrison (2016) and Section 4.2 means that

numerical predictions of θ_{wp} should be independent of mesh density, a point verified by a mesh sensitivity studies.

5.6.2 Determination of Torsional Stiffness of Sheared Fabric by Inverse Modelling of the Wrinkle Onset Angle

Finally, the torsional stiffness per unit width in each fibre direction, μ_i, of the sheared fabric was estimated via inverse modelling, while taking care to avoid early wrinkling due to inertial effects (see Section 5.6.1). The strategy is to adjust μ_i, (here $\mu_1 = \mu_2$) used in simulations of the UBE test in order to reproduce the observed wrinkle onset angle, θ_{we}, for the different sized specimens, i.e. to match θ_{wp} with θ_{we}. To this end, the tensile line stiffness per unit width in each fibre direction was fixed at 600KNm^{-1}, the out-of-plane bending stiffness per unit width in each fibre direction, β_i, was set to the values shown in Table 1, the shear force per unit length, $\mathrm{F_{sh}}(\theta)$, was determined using the polynomials of Table 2, and the in-plane bending stiffness was set with, $\alpha_h = 2\beta_h$, as suggested by the analysis of Section 5.5. The torsional stiffness was varied such that, $\xi_i = 1$, 6, 14 and 100 (i.e. the torsional stiffness was reduced to 1/6th, 1/14th and 1/100th of its initial default value). The results are indicated by the blue lines in Figure 7a and 7b and show that θ_{wp} is sensitive to changes in the torsional stiffness. As with the experimental wrinkle onset angle, θ_{we}, there is a reduction in θ_{wp} with increasing specimen size and θ_{wp} is higher for the treated fabric than the untreated fabric. Results suggest values of ξ_i of about 14 for both the untreated and the treated fabric provides a reasonable fit with the experimental data. Perhaps surprisingly, this value of ξ_i is the same as the value found for the un-sheared fabric determined from cantilever bending tests (see Section 5.3) suggesting that the torsional stiffness of this particular carbon fabric remains fairly constant during shear. This suggests that the torsional stiffness of the sheared fabric might be estimated from inverse modelling of the cantilever bending test; a much faster route than via inverse modelling of the UBE test. However, the generality of this point has yet to be shown for all fabrics.

Using the set of mechanical properties determined through the measurement and fitting process discussed in Section 5, the form of the wrinkles produced by the simulations for each specimen size and for both the untreated and treated fabrics is examined in Figure 16. Each image shows the UBE test simulation cut through the mid-section of the specimen and is produced when the centre of the specimen reaches a shear angle of 55^{o}. Figure 16 reveals

that the amplitude of the wrinkle increases with increasing specimen size and the wrinkles tend to be larger for the untreated fabric (Figures 16a-c), than the treated fabric (Figure 16d-f). These observations follow the same trends observed in experiments (see, for example, Figures 9-11). The direction of the out-of-plane displacement of the wrinkle changes randomly in the different simulations.

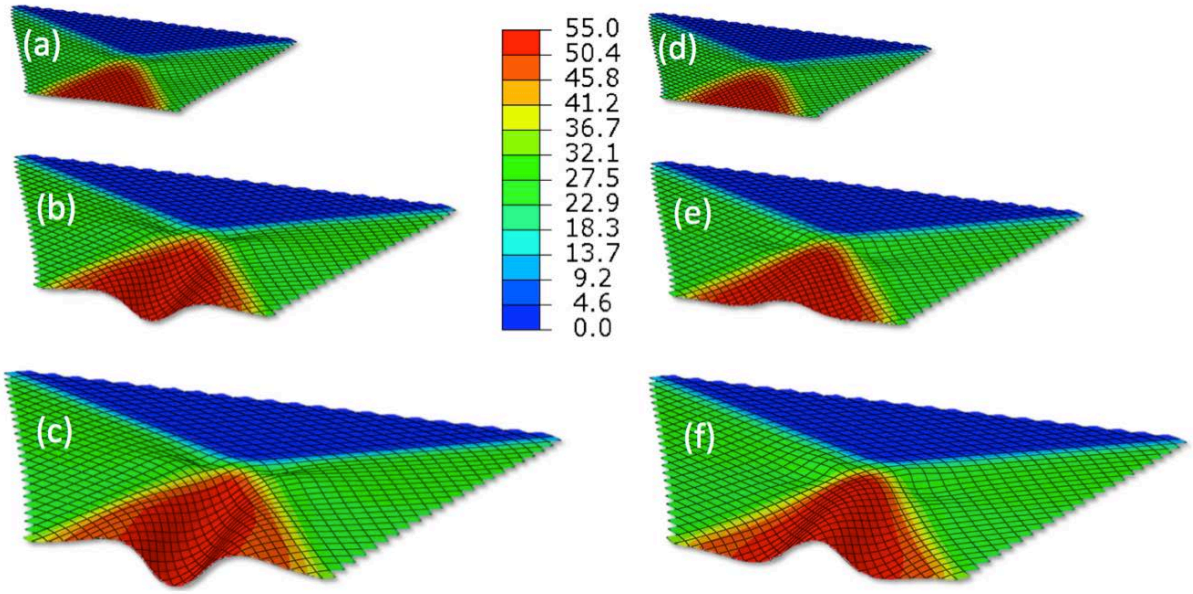

Figure 16. Specimen size dependent form of wrinkles occurring in the UBE test simulations, using the mechanical parameters determined following the procedures discussed in Section 5. Each image shows the UBE test simulation cut through the mid-section of the specimen when the shear angle at the centre of the specimen is 55^{o}. (a-c) produced using parameters measured for the untreated specimens, shown in order of increasing specimen size and (d-f) produced using parameters measured for the treated specimens, again shown in order of increasing specimen size. The legend indicates the shear angle.

Once again, in order to adopt this torsional stiffness fitting procedure with confidence, it is important to understand the sensitivity of the predicted wrinkle onset angle, θ_{wp}, to changes in the in-plane bending stiffness, α_i. In a first set of simulations, the torsional stiffness per unit width in each fibre direction, μ_i, was initially set with $\xi_i = 1$ (resulting in a relatively high torsional stiffness) and the in-plane bending stiffness was varied such that $\alpha_h = 0.5\beta_h, \beta_h, 2\beta_h$ & $3\beta_h$ where β_h is the higher of the two measured values (see Table 1). θ_{wp} predicted by these simulations, for each specimen size, is given by the red lines in

Figure 7a (untreated fabric) and 7b (treated fabric). θ_{wp} was found to be relatively insensitive to the value of the in-plane bending stiffness, α_i when the torsional stiffness was set at this high value. However, higher sensitivity to changes in α_h was observed when using a lower value of the torsional stiffness, e.g. with $\xi_i = 14$, results not shown in Figure 7. This implies that it is better to determine the torsional stiffness via inverse modelling of the UBE test only after values of the in-plane bending stiffness have been found (see Section 5.5).

6 Conclusions

A systematic approach to determining a comprehensive set of mechanical forming properties for engineering fabrics has been demonstrated. Just two experiments are required, the cantilever bending test and a modified version of the UBE test. The sensitivities of the experimental measurements to the various mechanical properties of the fabric suggest a natural order for the characterisation process, summarised as follows:

1. approximate the line stiffness per unit width, γ_i, in each fibre direction to ensure that tensile strains are limited to less than 1% in the UBE simulations (600 KNm^{-1} is usually high enough)
2. determine the out-of-plane bending stiffness per unit width in each fibre direction, β_i, directly from the cantilever bending test results (with the test specimens cut along the warp and weft directions)
3. determine the shear force per unit length, $F_{sh}(\theta)$, directly from UBE tests using stress-power normalisation theory. Larger specimen sizes are most suited to this task as they more closely adheres to ideal kinematics
4. set γ_i, β_i & $F_{sh}(\theta)$ using steps 1, 2 & 3. Estimate $\alpha_i = 2 \times \beta_h$. Simulate the cantilever bending test with the test specimens cut along the bias direction adjusting the torsional stiffness per unit width in each fibre direction, μ_i, until the observed and predicted bend angle match to within a given tolerance, e.g. 1.5%
5. set γ_i, β_i, $F_{sh}(\theta)$ & μ_i using steps 1, 2, 3 & 4. Simulate the UBE test, begin with the in-plane bending stiffness per unit width in each fibre direction $\alpha_i = 2 \times \beta_h$ and adjust until the simulated and measured shear kinematics match. Smaller specimen sizes are best suited to this task as they adhere to ideal kinematics least closely (they

are more sensitive to in-plane bending stiffness). Tests using multiple specimen sizes improve confidence in the fitting process

6. set γ_i, β_i, $F_{sh}(\theta)$ & μ_i using steps 1, 2, 3, 4 & 5. Simulate the UBE test adjusting the torsional stiffness per unit width in each fibre direction, μ_i, until the simulated and measured wrinkle onset angles match. This may produce a different value of μ_i to step 4.

Advantages of the modelling approach are that it is comprehensive and intuitive and since it is implemented in Abaqus Explicit™, it harnesses the full power and functionality of a mature commercial finite element code. A current limitation of the model is that many of the properties are assumed to be constant, whereas experimental evidence shows this is not the case. For example, the tensile modulus of woven fabrics is influenced by crimp-interchange, e.g. (Boisse et al., 2001; Potluri and Thammandra, 2007), and the out-of-plane bending modulus of engineering textiles is known to be a function of bending curvature (de Bilbao et al., 2010; Liang et al., 2014; Lomov et al., 2003). Methods of including non-linearity in the bending behaviour are possible, for example, the transverse modulus of the beam elements could perhaps be linked to the curvature of the beam. Currently, only a single constant value of the torsional stiffness can be used in any given simulation. As a result, if the value of μ_i found from steps 4 and 6 of the characterisation process is different, a decision must be made regarding the optimum value of μ_i for use in complex forming simulations. Another drawback is the need for a bespoke mesh generator (Abdiwi et al., 2012; Harrison, 2016) making it difficult to apply techniques such as adaptive meshing, though development of generalised continuum theory capable of including all the properties listed in Section 1, including in-plane bending stiffness (2nd order gradient effects) and torsional stiffness, is already under development, e.g. (Steigmann and Dell'Isola, 2015) and if implemented in shell elements may provide an alternative approach in future.

The advantage of the characterisation approach is that it is relatively simple, extending the utility of existing test methods to provide additional information with little extra effort. Unlike complex forming simulations, the method focusses purely on the material behaviour, providing a rigorous evaluation of the forming and wrinkling mechanics without introducing extra complications such as friction, complex boundary conditions and complex geometries, all of which can influence the fabric's wrinkling response. A disadvantage is that inverse

modelling of the UBE tests is a time-consuming process as simulations must be free from the undesirable influence of inertial effects, leading to long run-times. Though characterisation is required only once per material, thus, eventually a database of material behaviours will mitigate this disadvantage.

Stereoscopic DIC has been shown to be a useful tool in measuring the wrinkle onset angle in UBE tests, though care must be taken to quantify the influence that the sample treatment exerts on the resulting mechanical forming properties. In the current study, treatment of the fabric for DIC analysis significantly increased the wrinkle onset angle by around 10^{o}, suggesting that simple treatment of engineering fabrics could possibly enhance their resistance to wrinkling during the forming process. There remains considerable scope to further evaluate the in-plane bending stiffness of fabrics via comparison of experimental measurement and numerical predictions of full-field shear angle distributions. This may prove a viable route to measuring possible non-linearity of the in-plane bending stiffness as a function of in-plane curvature in the future.

Ultimately, the aim is to employ this modelling technique in complex forming simulations. Now that a concise, systematic approach to determining all the relevant mechanical properties has been demonstrated, forming simulations provide an interesting next step for future work.

Acknowledgments

This research did not receive any specific grant from funding agencies in the public, commercial, or not-for-profit sectors.

Appendix A: Influence of Bonded Aluminium as a Function of Specimen Size

As mentioned in Section 3.3, the main goal of bonding aluminium foil is to mitigate sample deformation in Region C and to provide a well-defined boundary condition along the edge of Region C. Before embarking on the main investigation the effects of bonding aluminium on the test specimen as a function of sample size were briefly examined. To do this, a preliminary series of UBE tests, with and without bonded aluminium, using plain woven

glass fabric specimens (Alscot, product code = ECK12 with warp & weft tow width of 2.12 ±0.052 & 2.18 ±0.038 mm respectively and an areal density of 339.6 +/- 0.3 gm^{-2}), of different sizes but the same aspect ratio ($\lambda = 2$), were conducted and revealed that: (a) no obvious difference in the experimentally determined wrinkle onset angle, θ_{we}, could be discerned between the bonded and un-bonded specimens, (b) larger test specimens generated significantly higher maximum normalised axial forces prior to loss of fabric integrity (a similar result was reported recently in (Pan et al., 2015)) and the bonded aluminium has no noticeable influence on this maximum value, see Figure A1(i), and (c) the normalised displacement (d/L_A) corresponding to the maximum axial force, prior to loss of fabric integrity, was significantly reduced by the presence of the bonded aluminium for all specimen sizes and was independent of specimen size, see Figure A1(ii); both points attributable to mitigation of intra-ply slip in Region C (Bel et al., 2012; Harrison et al., 2005; Pan et al., 2015; Potter, 2002). No adverse effects were noted in bonding the aluminium to the specimen, aside from the observation that greater care was required in preparing the samples in order to reduce variability in the experimental results.

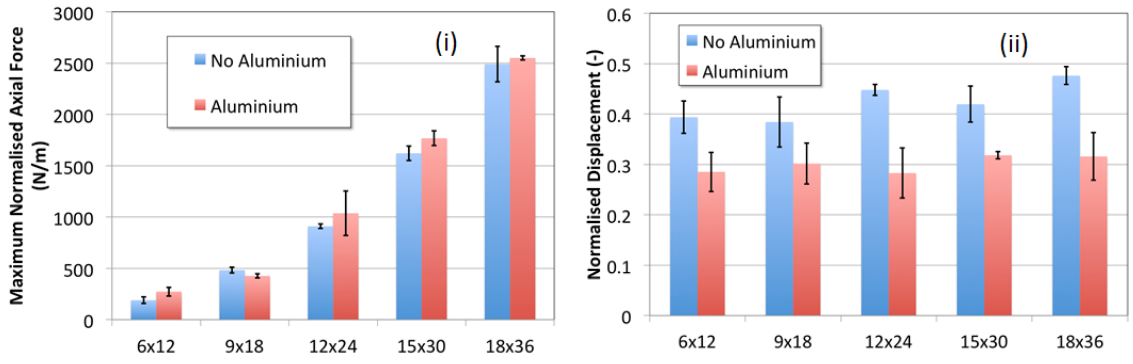

Figure A1. (i) Maximum axial force versus specimen dimensions for bonded and un-bonded glass fabric specimens (ii) normalised displacement at maximum axial force. All date were normalised by side length of Region A, L_A.

References

Abaqus User's Manual 6.14.

Abdiwi, F., Harrison, P., Koyama, I., Yu, W.R., Long, A.C., Corriea, N., Guo, Z., 2012. Characterising and modelling variability of tow orientation in engineering fabrics and textile composites. Compos. Sci. Technol. 72, 1034–1041. doi:10.1016/j.compscitech.2012.03.017

Arnold, S.E., Sutcliffe, M.P.F., Oram, W.L.A., 2016. Experimental measurement of wrinkle formation during draping of non-crimp fabric. Compos. Part A Appl. Sci. Manuf. 82, 159–169. doi:10.1016/j.compositesa.2015.12.011

Bel, S., Hamila, N., Boisse, P., Dumont, F., 2012. Finite element model for NCF composite reinforcement preforming: Importance of inter-ply sliding. Compos. Part A Appl. Sci. Manuf. 43, 2269–2277. doi:10.1016/j.compositesa.2012.08.005

Boisse, P., Gasser, A., Hivet, G., 2001. Analyses of fabric tensile behaviour: Determination of the biaxial tension-strain surfaces and their use in forming simulations. Compos. - Part A Appl. Sci. Manuf. 32, 1395–1414. doi:10.1016/S1359-835X(01)00039-2

Boisse, P., Hamila, N., Guzman-Maldonado, E., Madeo, A., Hivet, G., Dell???Isola, F., 2016. The bias-extension test for the analysis of in-plane shear properties of textile composite reinforcements and prepregs: a review. Int. J. Mater. Form. 1–20. doi:10.1007/s12289-016-1294-7

Boisse, P., Hamila, N., Vidal-Salle, E., Dumont, F., 2011. Simulation of wrinkling during textile composite reinforcement forming. Influence of tensile, in-plane shear and bending stiffnesses. Compos. Sci. Technol. 71, 683–692. doi:10.1016/j.compscitech.2011.01.011

Cao, J., Akkerman, R., Boisse, P., Chen, J., Cheng, H.S., de Graaf, E.F., Gorczyca, J.L., Harrison, P., Hivet, G., Launay, J., Lee, W., Liu, L., Lomov, S. V., Long, A., de Luycker, E., Morestin, F., Padvoiskis, J., Peng, X.Q., Sherwood, J., Stoilova, T., Tao, X.M., Verpoest, I., Willems, A., Wiggers, J., Yu, T.X., Zhu, B., 2008. Characterization of mechanical behavior of woven fabrics: Experimental methods and benchmark results. Compos. Part A Appl. Sci. Manuf. 39, 1037–1053. doi:10.1016/j.compositesa.2008.02.016

Carvelli, V., Pazmino, J., Lomov, S. V., Verpoest, I., 2012. Deformability of a non-crimp 3D orthogonal weave E-glass composite reinforcement. Compos. Sci. Technol. 73, 9–18. doi:10.1016/j.compscitech.2012.09.004

Chen, Z.R., Ye, L., 2006. A micromechanical compaction model for woven fabric preforms. Part II: Multilayer. Compos. Sci. Technol. 66, 3263–3272. doi:10.1016/j.compscitech.2005.07.010

Cherouat, A., Billoët, J.L., 2001. Mechanical and numerical modelling of composite manufacturing processes deep-drawing and laying-up of thin pre-impregnated woven fabrics. J. Mater. Process. Technol. 118, 460–471. doi:10.1016/S0924-0136(01)00987-6

Cooper, D.N.E., 1960. The Stiffness of Woven Textiles. J. Text. Inst. Trans. 51, T317–T335. doi:10.1080/19447026008659775

D'Agostino, M. V., Giorgio, I., Greco, L., Madeo, A., Boisse, P., 2015. Continuum and discrete models for structures including (quasi-) inextensible elasticae with a view to the design and modeling of composite reinforcements. Int. J. Solids Struct. 59, 1–17. doi:10.1016/j.ijsolstr.2014.12.014

Dangora, L.M., Mitchell, C.J., Sherwood, J.A., 2015. Predictive model for the detection of out-of-plane defects formed during textile-composite manufacture. Compos. Part A Appl. Sci. Manuf. 78, 102–112. doi:10.1016/j.compositesa.2015.07.011

de Bilbao, E., Soulat, D., Hivet, G., Gasser, A., 2010. Experimental Study of Bending Behaviour of Reinforcements. Exp. Mech. 50, 333–351. doi:10.1007/s11340-009-9234-9

Dell'Isola, F., Steigmann, D., 2014. A Two-Dimensional Gradient-Elasticity Theory for Woven Fabrics. J. Elast. 118, 113–125. doi:10.1007/s10659-014-9478-1

Ferreira, T., Rasband, W., 2012. ImageJ User Guide, Image J user Guide. doi:10.1038/nmeth.2019

Ferretti, M., Madeo, A., dell'Isola, F., Boisse, P., 2014. Modeling the onset of shear boundary layers in fibrous composite reinforcements by second-gradient theory. Zeitschrift fur Angew. Math. und Phys. 65, 587–612. doi:10.1007/s00033-013-0347-8

Gatouillat, S., Bareggi, A., Vidal-Salle, E., Boisse, P., 2013. Meso modelling for composite preform shaping - Simulation of the loss of cohesion of the woven fibre network. Compos. Part A Appl. Sci. Manuf. 54, 135–144. doi:10.1016/j.compositesa.2013.07.010

Giorgio, I., 2016. Numerical identification procedure between a micro-Cauchy model and a macro-second gradient model for planar pantographic structures. Zeitschrift für Angew. Math. und Phys. 67, 95. doi:10.1007/s00033-016-0692-5

Giorgio, I., Della Corte, A., Dell'Isola, F., Steigmann, D.J., 2016. Buckling modes in pantographic lattices. Comptes Rendus Mécanique. doi:10.1016/j.crme.2016.02.009

Harrison, P., 2016. Modelling the forming mechanics of engineering fabrics using a mutually constrained pantographic beam and membrane mesh. Compos. Part A Appl. Sci. Manuf. 81, 145–157. doi:10.1016/j.compositesa.2015.11.005

Harrison, P., Abdiwi, F., Guo, Z., Potluri, P., Yu, W.R., 2012. Characterising the shear-tension coupling and wrinkling behaviour of woven engineering fabrics. Compos. Part A Appl. Sci. Manuf. 43, 903–914. doi:10.1016/j.compositesa.2012.01.024

Harrison, P., Hartel, F., 2016. Erratum: "Evaluation of normalisation methods for uniaxial bias extension tests on engineering fabrics" (Composites: Part A (2016) 80 (104-106)). Compos. Part A Appl. Sci. Manuf. 80, 104–106. doi:10.1016/j.compositesa.2015.10.013

Harrison, P., Tan, M.K., Long, a C., 2005. Kinematics of Intra-Ply Slip in Textile Composites during Bias Extension Tests, in: 8th Int. ESAFORM Conf. on Materials Forming. Cluj-Napoca, Romania, pp. 2–5.

Harrison, P., Wiggers, J., Long, A.C., 2008. Normalization of Shear Test Data for Rate-independent

Compressible Fabrics. J. Compos. Mater. 1–30. doi:10.1177/0021998308095367

Harrison, P., Yu, W.R., Long, A.C., 2011. Rate dependent modelling of the forming behaviour of viscous textile composites. Compos. Part A Appl. Sci. Manuf. 42, 1719–1726. doi:10.1016/j.compositesa.2011.07.026

Hu, J., 2004. Structure and mechanics of woven fabrics, 1st ed. Woodhead Publishing Limited, Cambridge. doi:10.1017/CBO9781107415324.004

ISO, B.E., 1998. Textiles — Test methods for nonwovens Part 7: Determination of bending length.

Lammens, N., Kersemans, M., Luyckx, G., Van Paepegem, W., Degrieck, J., 2014. Improved accuracy in the determination of flexural rigidity of textile fabrics by the Peirce cantilever test (ASTM D1388). Text. Res. J. 84, 1307–1314. doi:10.1177/0040517514523182

Liang, B., Hamila, N., Peillon, M., Boisse, P., 2014. Analysis of thermoplastic prepreg bending stiffness during manufacturing and of its influence on wrinkling simulations. Compos. Part A Appl. Sci. Manuf. 67, 111–122. doi:10.1016/j.compositesa.2014.08.020

Lomov, S.V., Truevtzev, a. V., Cassidy, C., 2000. A Predictive Model for the Fabric-to-Yarn Bending Stiffness Ratio of a Plain-Woven Set Fabric. Text. Res. J. 70, 1088–1096. doi:10.1177/004051750007001208

Lomov, S. V., Verpoest, I., 2006. Model of shear of woven fabric and parametric description of shear resistance of glass woven reinforcements. Compos. Sci. Technol. 66, 919–933. doi:10.1016/j.compscitech.2005.08.010

Lomov, S. V., Verpoest, I., Barburski, M., Laperre, J., 2003. Carbon composites based on multiaxial multiply stitched preforms. Part 2. KES-F characterisation of the deformability of the preforms at low loads. Compos. Part A Appl. Sci. Manuf. 34, 359–370. doi:10.1016/S1359-835X(03)00025-3

Machado, M., Murenu, L., Fischlschweiger, M., Major, Z., 2016. Analysis of the thermomechanical shear behaviour of woven-reinforced thermoplastic-matrix composites during forming. Compos. Part A Appl. Sci. Manuf. 86, 39–48. doi:10.1016/j.compositesa.2016.03.032

Pan, N., Kovar, R., Dolatabadi, M.K., Wang, P., Zhang, D., Sun, Y., Chen, L., 2015. Origin of tensile strength of a woven sample cut in bias directions. R. Soc. Open Sci. 2, 1–18. doi:10.1098/rsos.140499

Pazmino, J., Carvelli, V., Lomov, S. V., 2014. Micro-CT analysis of the internal deformed geometry of a non-crimp 3D orthogonal weave E-glass composite reinforcement. Compos. Part B Eng. 65, 147–157. doi:10.1016/j.compositesb.2013.11.024

Pazmino, J., Mathieu, S., Carvelli, V., Boisse, P., Lomov, S. V., 2015. Numerical modelling of forming of a non-crimp 3D orthogonal weave E-glass composite reinforcement. Compos. Part A Appl. Sci. Manuf. 72, 207–218. doi:10.1016/j.compositesa.2015.02.013

Peirce, F.T., 1930. The “Handle” of Cloth As a Measurable Quantity. J. Text. Inst. Trans. 21, T377–T416. doi:10.1080/19447023008661529

Pierce, R.S., Falzon, B.G., Thompson, M.C., Boman, R., 2015. A low-cost digital image correlation technique for characterising the shear deformation of fabrics for draping studies. Strain 51, 180–189. doi:10.1111/str.12131

Plaut, R.H., 2015. Formulas to determine fabric bending rigidity from simple tests. Text. Res. J. 85, 884–894. doi:10.1177/0040517514553877

Potluri, P., Thammandra, V.S., 2007. Influence of uniaxial and biaxial tension on meso-scale geometry and strain fields in a woven composite. Compos. Struct. 77, 405–418. doi:10.1016/j.compstruct.2006.10.005

Potter, K., 2002. Bias extension measurements on cross-plied unidirectional prepreg. Compos. - Part A Appl. Sci. Manuf. 33, 63–73. doi:10.1016/S1359-835X(01)00057-4

Rashidi, A., Milani, A.S., 2016. CHARACTERIZATION OF WRINKLING AND DE-WRINKLING BEHAVIOUR OF WOVEN FABRICS USING A MULTI-STEP BIAXIAL BIAS EXTENSION TEST, in: ECCM17 - 17th European Conference on Composite Materials. Munich, Germany, pp. 26–30.

Sachs, U., Akkerman, R., Fetfatsidis, K., Vidal-Sall??, E., Schumacher, J., Ziegmann, G., Allaoui, S., Hivet, G., Maron, B., Vanclooster, K., Lomov, S. V., 2014. Characterization of the dynamic friction of woven fabrics: Experimental methods and benchmark results. Compos. Part A Appl. Sci. Manuf. 67, 289–298. doi:10.1016/j.compositesa.2014.08.026

Scerrato, D., Zhurba Eremeeva, I.A., Lekszycki, T., Rizzi, N.L., 2016. On the effect of shear stiffness on the plane deformation of linear second gradient pantographic sheets. ZAMM - J. Appl. Math. Mech. / Zeitschrift für Angew. Math. und Mech. 12, 1–12. doi:10.1002/zamm.201600066

Sharma, S.B., Sutcliffe, M.P.F., 2004. A simplified finite element model for draping of woven material. Compos. Part A Appl. Sci. Manuf. 35, 637–643. doi:10.1016/j.compositesa.2004.02.013

Steigmann, D.J., Dell’Isola, F., 2015. Mechanical response of fabric sheets to three-dimensional bending, twisting, and stretching. Acta Mech. Sin. Xuebao 31, 373–382. doi:10.1007/s10409-015-0413-x

ten Thije, R.H.W., Akkerman, R., 2009. A multi-layer triangular membrane finite element for the forming simulation of laminated composites. Compos. Part A Appl. Sci. Manuf. 40, 739–753. doi:10.1016/j.compositesa.2009.03.004

Thompson, A., Belnoue, J.P., Hallett, S.R., 2016. Numerical Modelling of Defect Generation During Preforming of Multiple Layers of 2D Woven Fabrics, in: ECCM17 - 17th European Conference on Composite Materials. Munich, Germany, pp. 26–30.

Turco, E., dell'Isola, F., Cazzani, A., Rizzi, N.L., 2016. Hencky-type discrete model for pantographic structures: numerical comparison with second gradient continuum models. Zeitschrift für Angew. Math. und Phys. 67, 85. doi:10.1007/s00033-016-0681-8

Willems, A., Lomov, S. V., Verpoest, I., Vandepitte, D., 2009. Drape-ability characterization of textile composite reinforcements using digital image correlation. Opt. Lasers Eng. 47, 343–351. doi:10.1016/j.optlaseng.2008.03.012